Department of Physics and Astronomy

University of Heidelberg

Bachelor thesis

in Physics

submitted by

Arthur Bolz

born in Filderstadt

2012

Measurement of the Relative Branching Fraction

$$\frac{\mathcal{B}(B_s^0 \to J/\psi f_2'(1525))}{\mathcal{B}(B_s^0 \to J/\psi \phi)}$$

of the Decay Mode $B_s^0 \to J/\psi f_2'(1525)$

with Respect to $B_s^0 \to J/\psi \phi$

This bachelor thesis has been carried out by Arthur Bolz

at the

Physikalische Institut

under the supervision of

Herrn Prof. Ullrich Uwer

Messung des Zerfallsratenverhältnisses $\mathcal{B}(B_s^0 \to J/\psi f_2'(1525))/\mathcal{B}(B_s^0 \to J/\psi\phi)$ des Zerfallskanals $B_s^0 \to J/\psi f_2'(1525)$ in Bezug zum Kanal $B_s^0 \to J/\psi\phi$:

Der Zerfall eines B_s^0 Mesons in den Endzustand $J/\psi(\mu^+\mu^-)K^+K^-$ wird mittels Daten die einer Luminosität von 1fb^{-1} entsprechen untersucht. Die Daten wurden im Jahre 2011 am LHCb-Experiment aufgezeichnet. Zusätzlich zu nichtresonanten Dreikörperzerfällen $B_s^0 \to J/\psi K^+K^-$ werden die zwei Zerfallskanäle $B_s^0 \to J/\psi\phi$ und $B_s^0 \to J/\psi f_2'(1525)$ beobachtet. In der vorliegenden Analyse werden $N_{f_2'} = 2187 \pm 111$ und $N_\phi = 13519 \pm 149$ Zerfälle dieser Art selektiert. Um von diesem Ergebnis auf die Zahl der tatsächlich produzierten Ereignisse zu schließen muss mit einer Effizienz korrigiert werden. Diese wird anhand simulierter Daten berechnet und unterscheidet sich leicht für die beiden betrachteten Kanäle. Die gemessenen Werte sind: $\epsilon_{f_2'} = (0.93 \pm 0.01)\%$ and $\epsilon_\phi = (1.10 \pm 0.03)\%$. Als abschließendes Ergebnis wird die relative Zerfallsrate der beiden Kanäle $\mathcal{B}(B_s^0 \to J/\psi f_2'(1525))/\mathcal{B}(B_s^0 \to J/\psi\phi) = (21.07 \pm 1.26(stat.)^{+2.63}_{-1.54}(yields) \pm 0.58(PDG))$ % gemessen.

Measurement of the Relative Branching Fraction $\mathcal{B}(B_s^0 \to J/\psi f_2'(1525))/\mathcal{B}(B_s^0 \to J/\psi\phi)$ of the Decay Mode $B_s^0 \to J/\psi f_2'(1525)$ with Respect to the Mode $B_s^0 \to J/\psi\phi$:

The decay of a B_s^0 meson into a $J/\psi(\mu^+\mu^-)K^+K^-$ final state is studied using data corresponding to 1fb^{-1} of integrated luminosity. The data was collected at the LHCb experiment in 2011. In addition to non-resonant 3-body decays $B_s^0 \to J/\psi K^+K^-$, decays by the two channels $B_s^0 \to J/\psi f_2'(1525)$ and $B_s^0 \to J/\psi\phi$ are observed. In this analysis $N_{f_2'} = 2187 \pm 111$ and $N_\phi = 13519 \pm 149$ of those events are selected. To determine the actual number of decays corresponding to the integrated luminosity those numbers have to be corrected with an efficiency. The efficiency is calculated from simulated data and has slightly different values for the two channels: $\epsilon_{f_2'} = (0.93 \pm 0.01)\%$ and $\epsilon_\phi = (1.10 \pm 0.03)\%$. As a final result the relative branching fraction $\mathcal{B}(B_s^0 \to J/\psi f_2'(1525))/\mathcal{B}(B_s^0 \to J/\psi\phi) = (21.07 \pm 1.26(stat.)^{+2.63}_{-1.54}(yields) \pm 0.58(PDG))$ % is measured.

Contents

1 Introduction

Particle physics aims to describe the fundamental building blocks of matter and their interactions. Our current knowledge culminates in the Standard Model of particle physics. It provides a framework of particles and interactions and has been successfully used to describe many of the observed phenomena.

However, many questions remain unanswered by the Standard Model. It cannot explain the dominance of matter over antimatter [1] or the nature of dark matter and dark energy that make up the largest part of the universe [2]. Also, the Higgs mechanism [3], which is widely used to describe the origin of the masses of particles, lacks a final experimental proof.

The Large Hadron Collider (LHC) at CERN was built to study those phenomena and to find evidence for new and advanced theories. In the high energy proton-proton collisions in the LHC all kinds of fundamental particles are created. These particles, as well as their interactions, can be studied with various highly sensitive detectors.

The analysis of this thesis is using data of the LHCb-experiment situated at the LHC. The main focus of the experiment is the precise study of particle-antiparticle asymmetry (CP violation[1]) for B and D mesons. The Standard Model already includes CP violation in the weak interaction but in order to explain the excess of matter it would have to be much larger than predicted. At LHCb, the properties of B and D mesons are measured with high accuracy in order to find discrepancies to the Standard Model predictions [4].

In this thesis the decay of a B_s^0 meson into a $J/\psi(\mu^+\mu^-)K^+K^-$ final state is investigated. CP violation in the B_s^0 system has been studied on the basis of the decay mode $B_s^0 \to J/\psi\phi(K^+K^-)$ for quite some time [4]. In addition the newly discovered channel $B_s^0 \to J/\psi f_2'(1525)$, which has the same final state, might be a candidate for similar analyses [5]. In this thesis the relative branching fraction of the decays $B_s^0 \to J/\psi f_2'(1525)$ and $B_s^0 \to J/\psi\phi$ is measured as a first step of analyzing the $B_s^0 \to J/\psi f_2'(1525)$ channel.

The relative branching fraction predominantly depends on the relative event yields of the decays $B_s^0 \to J/\psi f_2'(1525)$ and $B_s^0 \to J/\psi\phi$. Those yields are measured in Section 5. This is done by fitting the invariant mass distributions of be B_s^0 and the combined K^+K^-. The applied fitting methods are discussed in Section 2. In addition, a brief summary of the Standard Model of physics is given in that section to help better understand the considered decays. Section 3 gives a brief overview of the LHCb-detector. The data sample used for the analysis is introduced in Section 4. The event yields have to be corrected with an efficiency that is calculated in Section 6. For the calculation simulated data of the considered decays is used. This data is also discussed in Section 4.

[1] C is the quantum mechanical operator inverting charge, P, the parity operator, inverts space.

2 Theory

This section aims to give a short and phenomenological overview of the Standard Model of particle physics. It focuses mainly on the properties of hadrons. For more detailed information it is referred to the academic literature [6]. In addition a short introduction to maximum-likelihood fitting methods is given.

2.1 The Standard Model

The Standard Model of particle physics is the theory used to describe the building blocks of matter and their interactions. It is a relativistic quantum field theory combining both the Quantum Chromo Dynamics (QCD) [7] and the Glashow-Salam-Weinberg theory [8] [9] [10]. The QCD describe the strong interaction, whereas the Glashow-Salam-Weinberg theory gives a description of the unified weak and electromagnetic interaction. The Standard Model includes 12 spin-$\frac{1}{2}$ fermions, which are the matter particles, and 12 spin-1 gauge bosons that carry the fundamental forces. The fermions are divided into leptons and quarks that again are classified into three generations listed in Table 2.1. The interactions are compared in Table 2.2.

Table 2.1: Properties of the matter particles in the Standard Model [11].

Gen.	Flavor	Charge	Mass (MeV/c^2)	Particle	Charge	Mass (MeV/c^2)
1^{st}	$\begin{pmatrix} u \\ d \end{pmatrix}$	$+\frac{2}{3}$ $-\frac{1}{3}$	$2.3^{+0.7}_{-0.5}$ $4.8^{+0.7}_{-0.3}$	$\begin{pmatrix} e^- \\ \nu_e \end{pmatrix}$	-1 0	0.511 $< 2\ 10^{-6}$
2^{nd}	$\begin{pmatrix} c \\ s \end{pmatrix}$	$+\frac{2}{3}$ $-\frac{1}{3}$	$1.28 \pm 0.03\ 10^3$ 95 ± 5	$\begin{pmatrix} \mu^- \\ \nu_\mu \end{pmatrix}$	-1 0	105.7 <0.19
3^{rd}	$\begin{pmatrix} t \\ b \end{pmatrix}$	$+\frac{2}{3}$ $-\frac{1}{3}$	$160 - 173.5\ 10^3$ $4.18 - 4.65\ 10^3$	$\begin{pmatrix} \tau^- \\ \nu_\tau \end{pmatrix}$	-1 0	1776.8 ± 0.2 <18.2
	Quarks			Leptons		

Table 2.2: Properties of the interactions known to the Standard Model and the according gauge bosons [11].

Interaction	(Gauge) Boson	Mass	Relative Strength	Range
strong	8 gluons	0	1	< 1 fm
electromagnetic	photon (γ)	0	$\mathcal{O}(10^{-2})$	∞
weak	$W^{\pm}$, Z^0	80, 91 GeV/c^2	$\mathcal{O}(10^{-7})$	10^{-3}fm

All particles from Table 2.1 undergo the weak interaction and all except for the neutrinos ν interact electromagnetically. The strong force on the other hand only affects quarks. It acts on a quantum number called color that is possessed by both quarks and gluons. There are three colors charges that are commonly called red, green and blue and their according anti-colors. Quarks can change colors by exchanging

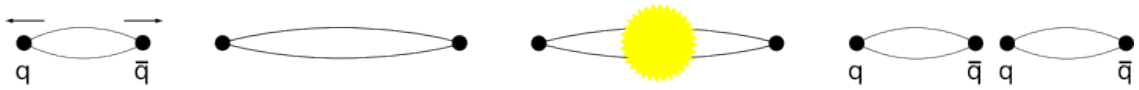

Figure 2.1: Illustration of hadronization due to confinement.

gluons. A consequence of the gluons carrying color, i.e., strongly interacting with each other, is the principle of confinement: It states that quarks can only persist within bound, color-neutral states called hadrons. In fact, trying to separate two quarks held together by the strong force leads to an increase in the strength of the potential with increasing distance. At some point it is energetically favorable for a new quark-antiquark pair to spontaneously appear out of the vacuum and form two new and color-neutral particles. See also Figure 2.1.

There are two different kinds of hadrons: baryons that have three valence quarks, i.e., quarks defining their quantum numbers, and mesons that consist of a quark and antiquark pair. Despite the small number of valence quarks, compared, for example to a lead atom with more than 200 nucleons, hadrons have to be imagined as very complex and dynamic objects. The quarks constantly exchange gluons some of which decay into quark-antiquark pairs. Those can interact with other quarks or simply annihilate each other again. The results is a "sea" of gluons and (anti-)quarks of all flavors surrounding the actual valence quarks.

Among the hadrons only protons(u, u, d) and neutrons(d, d, u) are stable and contribute to the matter that we know from our daily experience. All the others have a rather short lifetime of less than ∼26 ns ($\pi^{\pm}$) [11]. Eventually, they decay into lighter quarks and leptons. A direct consequence of this is the ambiguity of the masses of those hadrons. In order to understand this, it is instructive to look at the time dependent part of the wave function of a particle with mass $M_0 = E_0/c^2$ and lifetime τ, which is given in Equation (2.1). Performing a Fourier transform gives the probability density in energy space, i.e., the probability of having a certain energy or mass $M = E/c^2$ [12].

$$\psi(t) = e^{(iE_0 \cdot t/\hbar - t/2\tau)} \quad \Rightarrow \quad |\psi(t)|^2 = e^{-t/\tau} \tag{2.1}$$

$$|\psi(E)|^2 = |\frac{1}{\sqrt{2\pi}} \int_{-\infty}^{\infty} e^{i(E_0 - E)\cdot t/\hbar} \cdot e^{-t/\tau}\, dt|^2 = \frac{1}{2\pi} \cdot \frac{\hbar^2}{(E_0 - E)^2 + \Gamma^2/4} \tag{2.2}$$

According to Equation (2.2) this probability density is given by a Breit-Wigner function with width $\Gamma = \hbar/\tau$. More accurately it can be described by a relativistic Breit-Wigner function with an energy dependent width. The according formula is given in Equation (2.9) in Section 2.2 and will be used to describe the mass spectra of hadrons in this thesis.

Hadrons can be generated in particle collisions, such as those produced by the LHC. In the inelastic scattering of two high-energy protons, for example, a sea quark and antiquark from the two protons can annihilate. This can break the color neutrality of the protons and lead to their dissociation. The freed quarks scatter in all direc-

tions forcing the creation of new quarks from the vacuum due to the principle of confinement. At high energies many new quarks are created and jets of hadrons are formed. Due to their short lifetime most of those cannot be directly observed but quickly decay into lighter and longer-living hadrons and leptons. However, their existence and properties can be inferred from the decay products.

In this thesis the decay of a $B_s^0(\bar{b}s)$ meson into a $J/\psi(c\bar{c})$ meson and a $K^+(u\bar{s})K^-(\bar{u}s)$ meson pair is studied. An important source for B_s^0 mesons is the annihilation of a quark-antiquark pair in proton-proton collisions resulting in the emission of a high-energy gluon. The gluon can decay into a $b\bar{b}$ pair and the b ($\bar{b}$) quark can combine with a $\bar{s}$ (s) quark to form a B_s^0 ($\bar{B}_s^0$). See also Figure 2.2. In the considered final state the J/ψ decays into a μ^+ and μ^- lepton. The B_s^0 can either decay directly into $J/\psi K^+K^-$ or first decay into a J/ψ and either a $\phi(s\bar{s})$ meson or a $f_2'(1525)$ resonance that then decay into K^+K^-. However, muons and kaons are the first particles in the B_s^0 decay that actually live long enough to be directly observed. The presence of all other particles has to be inferred from their properties. The Feynman graph of lowest order for the $B_s^0 \to J/\psi\phi$ decay is given in Figure 2.2. It is a weak decay, i.e., it happens due to the exchange of a W boson. In contrast to strong decays where quark flavor is conserved, the weak decay can change one quark into another.

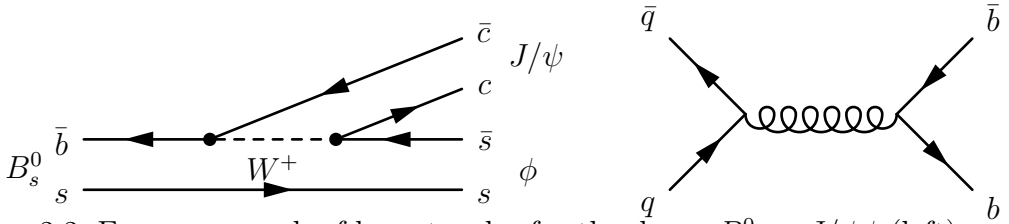

Figure 2.2: Feynman graph of lowest order for the decay $B_s^0 \to J/\psi\phi$ (left) and one example for the production of a $b\bar{b}$ pair (right).

2.2 Maximum-Likelihood Fitting and Definition of Probability Density Functions

In the course of the analysis performed in Section 5, it will be necessary to fit mathematical models to the measured data in order to extract relevant information. The relevant fitting methods will be briefly described in this section. In addition the parameterizations of the models used in Section 5 will be given.

In the following, a set $D(x_1, ..., x_N)$ of N equivalent values, e.g., the measured B_s^0 masses of N different events, will be considered. A probability density function (pdf) $P(x, \vec{\lambda})$ depending on M parameters $\vec{\lambda} = (\lambda_1, ..., \lambda_M)$ will be used to describe it. $P(x, \vec{\lambda})$ is a function of x where, for instance, x can represent a mass value. It assigns each allowed value a probability, i.e., if a data set was randomly generated according to the pdf, $P(x, \vec{\lambda})dx\%$ of the data points would lie in the interval

$[x, x + dx]$. Naturally $P(x, \vec{\lambda})$ has to be normalized over the allowed range, i.e.,

$$\int_{x_{min}}^{x_{max}} P(x; \vec{\lambda})\, dx = 1 \tag{2.3}$$

for each possible parameter set $\vec{\lambda}$.

As a measure quantifying the agreement between $D(x_1, ..., x_N)$ and the pdf the likelihood function can be defined as the product of all the probabilities assigned to the values in the set.

$$\mathcal{L}(\vec{\lambda}; D(x_1, ..., x_N)) = \prod_{i=1}^{N} P(x_i; \vec{\lambda}) \tag{2.4}$$

It is a function of $\vec{\lambda}$ and gives the probability to find the measured set $D(x_1, ..., x_N)$ under the assumption of the probability distribution $P(x, \vec{\lambda})$.

In a maximum-likelihood fit the parameters of the pdf are varied in order to find the values that provide the best agreement between $P(x; \vec{\lambda})$ and $D(x_1, ..., x_N)$. The likelihood function can be used to find those values because they should maximize it. Equivalently, it can be searched for a maximum in the logarithm of $\mathcal{L}(\vec{\lambda}; D(x_1, ..., x_N))$ which is much easier to handle numerically.

$$\ln \mathcal{L}(\vec{\lambda}; D(x_1, ..., x_N)) = \sum_{i=1}^{N} \ln P(x_i; \vec{\lambda}) \tag{2.5}$$

For technical reasons one searches for a minimum in $-\ln \mathcal{L}(\vec{\lambda}; D(x_1, ..., x_N))$.

Without any limitations this can be extended on multidimensional data sets and pdfs, e.g., when $x_i \to \vec{x_i}$ is a measure of several quantities like the measured masses of two different particles in an event.

In the following, the parameterizations of the pdfs used in the mass fits in Section 5 are discussed. They are all functions of x, which represents a mass in Section 5. The factor $\frac{1}{N}$ that appears in Equation (2.6), (2.7), (2.8) and (2.9) is a normalization factor to make sure that the pdfs are normalized. It is controlled by the fitting program that computes either the analytical or numerical integral over the fitted mass range.

Equation (2.6) gives the used parameterization of a polynomial of degree n that depends on the parameters $p_0, ...p_n$.

$$\mathcal{P}_n(x; p_0, ..., p_n) = \frac{1}{N} \left(p_0 + p_1 \cdot x + ... + p_n \cdot x^n\right) \tag{2.6}$$

It should be noted that due to the normalization condition the polynomial only has n free parameters (p_0 cancels out).

Equation (2.7) is a standard Gaussian distribution of the quantity x with width σ and mean μ.

$$\mathcal{G}(x;\mu,\sigma) = \frac{1}{N}\cdot e^{-\frac{(x-\mu)^2}{2\sigma^2}} \tag{2.7}$$

By combining two Gaussian functions the double Gaussian distribution given in Equation (2.8) is obtained.

$$\mathcal{DG}(x;\mu,\sigma_1,\sigma_2,f_G) = \frac{1}{N}\left(f_G\cdot e^{-\frac{(x-\mu)^2}{2\sigma_1^2}} + (1-f_G)\cdot e^{-\frac{(x-\mu)^2}{2\sigma_2^2}}\right) \tag{2.8}$$

f_G is the relative fraction used to weight one Gaussian with respect to the other. μ denotes again the mean value and is chosen the same for both parts. The two widths σ_1 and σ_2 can be different.

Table 2.3: Blatt-Weisskopf barrier factors used in the mass dependent width of a relativistic Breit-Wigner resonance [11].

Spin J	$B_J(z)^2$	$B'_J(z,z_0)^2$
0	1	1
1	$\frac{1}{1+z^2}$	$\frac{1+z_0^2}{1+z^2}$
2	$\frac{1}{9+3z^2+z^4}$	$\frac{9+3z_0^2+z_0^4}{9+3z^2+z^4}$

Equation (2.9) is a relativistic Breit-Wigner function used to describe the resonance shape of a particle with spin J decaying into two particles with masses m_a and m_b [11].

$$\mathcal{BW}(x;m_0,\Gamma_0,J,R,m_a,m_b) = \frac{1}{N}\frac{m_0^2\cdot\Gamma(x)^2}{(x^2-m_0^2)^2+m_0^2\cdot\Gamma(x)^2} \tag{2.9}$$

$$\Gamma(x) = \Gamma_0\left(\frac{p(x)}{p(m_0)}\right)^{2J+1}\left(\frac{m_0}{x}\right)B'_J(R\cdot p(x),R\cdot p(m_0))^2 \tag{2.10}$$

The mean value of the distribution is denoted with m_0 and Γ_0 is the parameter describing the physical width. The actual width is a function of x, i.e., the invariant mass of the particle, and is given in Equation (2.10). It depends on a quantity with the dimension of a length, R, the momentum of the particle, $p(x)$, and a barrier factor $B_J(z,z_0)$. R is commonly called the meson radius. $B_J(z,z_0)$ is given in Table 2.3 and $p(x)$ can be calculated with the masses of the decay products:

$$p(x) = \frac{x}{2}\left(1-\frac{(m_a+m_b)^2}{x^2}\right)^{1/2}\left(1-\frac{(m_a-m_b)^2}{x^2}\right)^{1/2}. \tag{2.11}$$

For further details on the the shape of mass resonances it is referred to the particle physics reviews provided by the PDG[2] [11].

3 The LHCb Experiment

The analysis performed in this thesis is based on data measured with the Large Hadron Collider beauty (LHCb) detector. LHCb [13] is one of the experiments at the Large Hadron Collider (LHC) [14] and is designed for the special purpose of reconstructing decays of B-mesons. The physics program focuses on the measurement of CP violation in B-meson systems and on indirect signs of particles and physics beyond the Standard Model. The detector design will be briefly discussed in this section a more detailed description can be found elsewhere [15].

3.1 The LHC

The LHC is at the time of writing the world's most powerful particle accelerator. It is operated by the European Organization for Nuclear Research (CERN) [16]

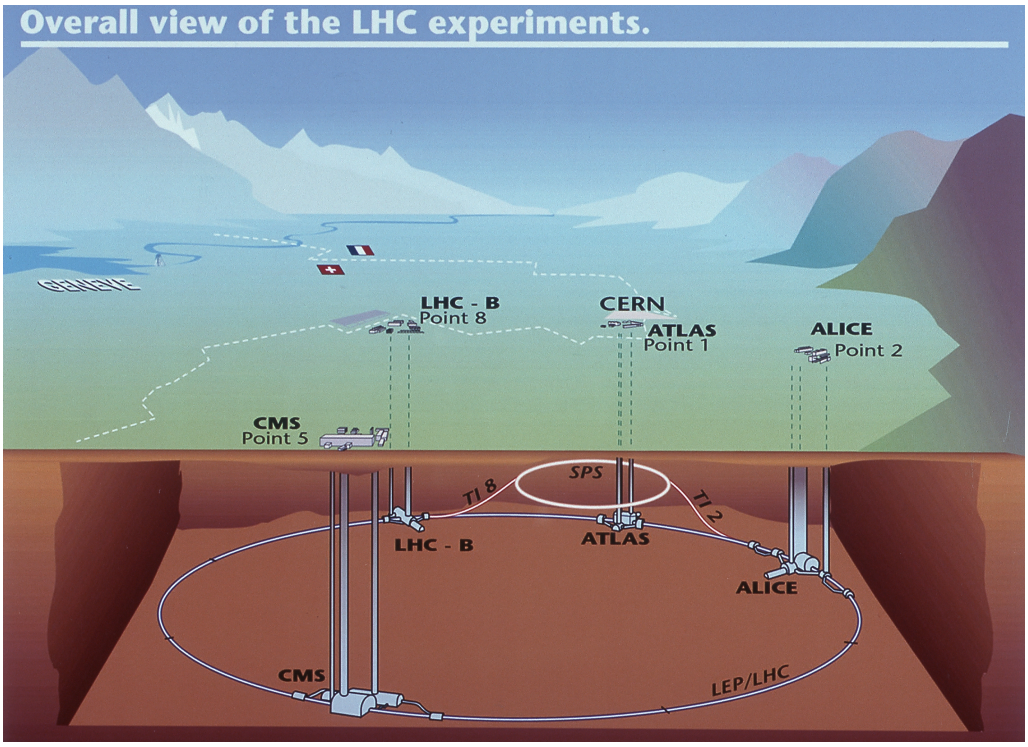

Figure 3.1: Overview over CERN's accelerator complex with the LHC and the associate experiments.[3]

near Geneva at the border between France and Switzerland. The main accelerator

[2]http://pdg.lbl.gov/2011/reviews/contents_sports.html (June 2012)

is circular with a circumference of approximately 27 kilometers and is built into a tunnel 175 meters below ground. It is designed to collide two oppositely running beams of either protons or lead ions. Originally, each proton was to be accelerated up to an energy of 7 TeV resulting in a center of mass energy of $\sqrt{s} = 14$ TeV. However, this energy has not been reached yet because of current technical limitations of the superconducting magnets. In 2011, when the data that is used in this thesis was measured, the LHC ran at $\sqrt{s} = 7$ TeV.

In addition to LHCb there are three other large experiments situated at the LHC. ATLAS (A Toroidal LHC Apparatus) and CMS (Compact Muon Solenoid) are two general purpose detectors designed for the search of the Higgs boson, heavy particles predicted by supersymmetry theories, the origin of dark matter and new physics in general. ALICE (A Large Ion Collider Experiment) is specialized on analyzing heavy ion collisions and on studying the resulting quark–gluon plasma. Figure 3.1[3] gives an overview over the LHC and the positions of the experiments.

3.2 The LHCb Detector

The design of the LHCb detector is highly influenced by its purpose of measuring B-decays [15]. b-$\bar{b}$-pairs, and consequently B-mesons, are predominantly produced in a rather narrow forward or backward cone. There is no need for a detector with full 4π coverage to study them and therefore the LHCb was built as a single arm forward spectrometer. It covers an angle between 10 to 300 mrad in the horizontal and between 10 to 250 mrad in the vertical plane. It is thus able to detect approximately 25% of the produced B-mesons. A cut through the detector along the z-y-plane is shown in Figure 3.2[4]. In the following a right-handed coordinate system is chosen with the z axis along beam axis and the y axis along the vertical.

The various parts of the detector can be subdivided into two classes pursuing two tasks:

- **Tracking:** The Vertex Locator (VELO) around the interaction point, the Trigger Tracker (TT) in front of the magnet and the 3 tracking stations (T1,T2, and T3) behind the magnet serve the purpose of measuring primary vertices and particle tracks. In addition with the magnet they also can be used to determine the momenta of particles.
- **Particle Identification:** Two Cherenkov detectors (RICH 1 and RICH 2) are used for separating pions, kaons and protons, each covering a different momentum spectrum. The electromagnetic (ECAL) and hadronic calorimeter (HCAL) help to identify electrons and photons, and the muon chambers (M_i) at the end of the detector detect muons.

The functionality of both classes of detectors is discussed in the following sections. In addition a third section describes the functionality of the LHCb trigger system that is used to reduce the data that is actually stored permanently.

[3]Picture from: https://cdsweb.cern.ch/record/40525 (June 2012)
[4]Picture from: https://cdsweb.cern.ch/record/1087860 (June 2012)

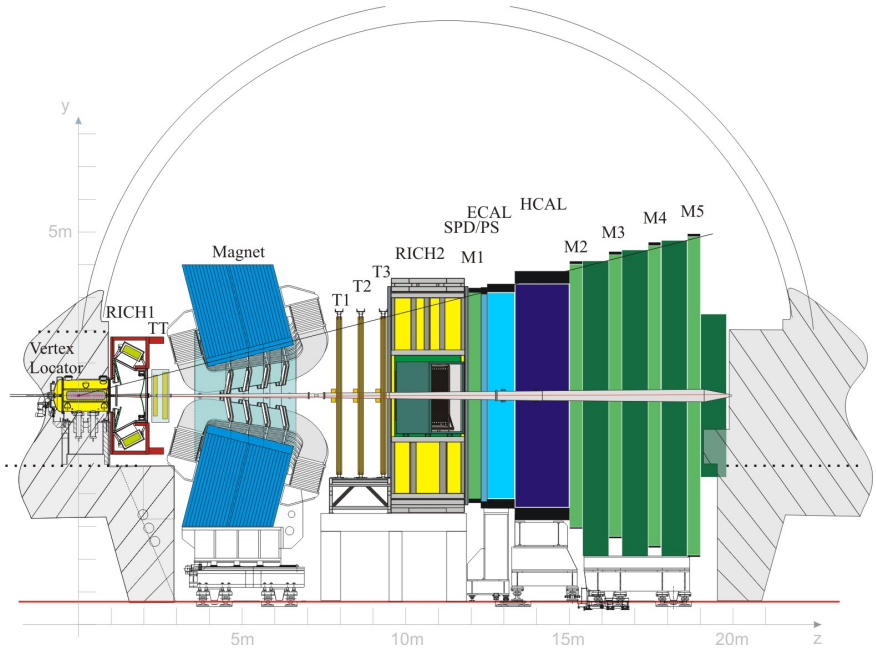

Figure 3.2: Side view of the LHCb detector to give an overview over its major components.[4]

Tracking[15, ch. 5]

Due to their short lifetime ($\sim$ 1.5 ps [11]) B-mesons decay before they hit any part of the detector. The VELO that is built around the collision point is used to measure their production and decay vertices with high accuracy. It consists of 42 semi-circular silicon microstrip detectors distributed along both sides of the beam axis. They are used to measure the distance to the z axis, r, and the angle in the x-y-plane, ϕ of decayed particles. The outstanding feature of the VELO is that it can be moved very close around the actual beam. This allows to determine the proton-proton collision point with an resolution of up to 50 μm. During proton injection at LHC, when the beams are unfocused, the VELO can be moved out from the beam axis for protection.
The Trigger Tracker and the T-stations measure particle tracks. Each of the T-stations consists of two different kinds of detectors. The rectangular inner parts, called Inner Tracker (IT), as well as the TT consist of two silicon strip detectors. They are rotated by 5° with respect to each other in order to provide a space resolution along the strips. The Outer Tracker (OT) is formed by the remaining parts of the T-stations which are drift chambers build from straw tubes. In the reconstruction process the hits in the tracking detectors are combined to full particle tracks.

In combination with the dipole magnet the tracking system can be used to measure momenta of charged particles. The magnet provides a bending strength of the order of $\int B\, dl = 4$ Tm [15, ch. 4]. A particle moving along the z axis is bent in the z-x

plane and the deflection gives information about its momentum.

Particle Identification [15, ch. 6]

Many of the observed B-meson decays at LHCb have kaon and pion final states. For a proper reconstruction it is important to distinguish these particles, which is done with two Ring Imaging Cherenkov (RICH) detectors. RICH1 covers the low momentum spectrum up to ∼60 GeV/c and is placed before the magnet because slow particles are deflected significantly by the magnetic field. RICH2, which is situated after the T-stations, covers higher momenta between 15 GeV/c and more than 100 GeV/c. The functionality of the RICH detectors is based on the Cherenkov effect: Particles moving through a medium at a speed higher than the phase velocity of light emit photons. Similar to the Mach cone produced by a supersonic sound source the photons are emitted in an angle θ depending on the particle's velocity $\beta = v/c$ and the refraction index of the medium, n [17]:

$$cos(\theta) = \frac{1}{n\beta} \ . \tag{3.1}$$

In principle θ can be measured and converted into the velocity. The velocity of a particle together with its momentum can then be used to determine its mass and, consequently, to identify it.

In practice, the information provided by the RICH detectors is used to calculate the probability that a particle is of a certain type. Usually, two probabilities are compared via the Delta Log Likelihood (DLL) value:

$$\mathrm{DLL}(K-\pi) = ln\mathcal{L}(K) - ln\mathcal{L}(\pi) = ln\frac{\mathcal{L}(K)}{\mathcal{L}(\pi)} \ . \tag{3.2}$$

Where $\mathcal{L}(K)$ ($\mathcal{L}(\pi)$) is the probability that the considered particle is a kaon (pion). For $\mathrm{DLL}(K-\pi) < 0$ the particle is more likely a pion and vice versa.

The actual purpose of the calorimeters is to measure energies of electrons and photons (ECAL) and hadrons (HCAL). But they also can be used for photon and electron identification.

Finally the muon chambers at the end of the detector are used for identifying and reconstructing muon tracks. Due to their large mass muons have a large mean free path and cross other parts of the detector without being measured.

Trigger [15, ch. 7]

At LHC proton bunches cross at a rate of up to 40 MHz and produce way more signals in the LHCb detector than can be handled and saved. In addition many of the events are of no interest because, for example, they do not contain B-decays. That's why a three level trigger system is used to select relevant events online and to reduce the data rate to about 2.2kHz.

B-decays are known to produce particles with relatively large transverse momenta with respect to the small transverse momenta of particles from "minimum bias" events. The first trigger level, the hardware based Level-0 (L0) trigger, extracts such events by applying various criteria to the calorimeters and the muon chamber signatures. The following High Level Trigger is a software trigger running on a large server farm. It consists of two stages: The HLT1 partially reconstructs events and confirms the decision of the L0. The HLT2 then does a full reconstruction similar to the offline reconstruction procedure. It applies several criteria in order to filter out uninteresting events and to classify the remaining ones according to various sets of requirements combined to so-called trigger lines. For this thesis the lines classifying events with a J/ψ decaying into two muons are of special interest. Further details are given in Section 4.3.

4 Reconstruction and Selection of the Data Sample

In this analysis the decay $B_s^0 \to J/\psi K^+K^-$ where the J/ψ decays into $\mu^+\mu^-$ is studied. It is thus necessary to obtain a data sample of suitable events from the recorded LHCb data. Preferably, the sample should be very clean, i.e., it should contain many signal events and as little background as possible. In order to achieve this the data is filtered in two stages. First the information of the online LHCb trigger system is used to get rid of events that are obviously of no interest for the analysis. Then only events are selected that meet certain requirements in the offline reconstruction process.

4.1 Data Taking Conditions

The data sample used for this analysis corresponds to approximately 1 fb^{-1} of integrated luminosity[5] and was collected with the LHCb detector in 2011. At the time the LHC was operated at a center-of-mass energy of the two colliding protons of $\sqrt{s} = 7$ TeV.

4.2 Trigger and Selection Requirements

This section gives a more detailed overview of the criteria for selection of the analysis data sample. The information provided by the LHCb trigger system is used as a first event filter. The relevant HLT trigger lines for this analysis are discussed in the following passage. Further below, the selection requirements in the reconstruction process are presented.

All events that pass any of the several trigger lines of the High Level Trigger (HLT1) are used. The second stage (HLT2) is then used to filter for events with a J/ψ

[5]The luminosity is a measure for the performance of the accelerator insofar, as the number of interactions is proportional to the integrated luminosity.

Table 4.1: Required trigger lines for the selection of the data sample for the analysis.

Triggerline	Hlt1Global & Hlt2DiMuonDetachedJPsi || Hlt2DiMuonJPsi
Requirements[18]	
μ track χ^2/ndf	< 5
$\mu^+\mu^-$ vertex χ^2/ndf_{vtx}	< 25
μ p_t	> 500 MeV/c

decaying into $\mu^+\mu^-$. The two used HLT2 trigger lines are listed in Table 4.1. They require two opposite sign tracks with hits in the muon chambers, a common vertex of the two muon candidates and an invariant $\mu^+\mu^-$ mass within ± 120 MeV/c^2 of the J/ψ mass. The fits of the tracks as well as the vertex have to be of good quality indicated by the χ^2/ndf value[6]. Events with a track $\chi^2/ndf_{track} > 5$ and a vertex $\chi^2/ndf_{vtx} > 25$ are cut away. In addition the Hlt2DiMuonDetachedJPsi line makes an implicit cut on the muon transverse momentum of $p_t > 500$ MeV/c.

In the reconstruction process two opposite sign tracks that are identified as muons in the muon chambers are combined to a J/ψ. Similarly, it is looked for two opposite sign kaons with a common vertex. The kaons can be identified using the particle identification (PID) criteria from the RICH detector. If the J/ψ and the K^+K^- system have a common vertex they are reconstructed to a B_s^0 candidate. For calculating the B_s^0 mass the J/ψ candidate's mass is constrained to the Particle Data Group (PDG) value [11].

From all the reconstructed events only a fraction is selected for the analysis data sample. Several cuts are applied in the selection process in order to enhance signal and reject background. They are summarized in Table 4.2. The specific values were taken from a similar analysis done by the LHCb Collaboration [5] and are known to provide a good signal to background ratio. This, however, was not analyzed in this thesis.

First of all, only tracks of good quality are considered, which is characterized by the χ^2/ndf_{track} value of the track fit through the hits in the detector. This suppresses random hits being wrongly combined to a particle track. In addition there are further reconstruction quality requirements and some kinematic cuts. Especially noteworthy are the cuts on the kaon PID variables DLL$(K-\pi)$ and DLL$(p-K)$. The inclusive decays $B \to J/\psi X$, where X is anything, contains a lot of pion final states. In some cases like for $B^0 \to J/\psi K_2^\star$ with $K_2^\star \to K\pi$ misidentifying the π as a K can shift the B mass into the range of the B_s^0 mass [5]. Consequently, there is no way of distinguishing such background events from true $B_s^0 \to J/\psi K^+K^-$ decays. To reject them, DLL$(K-\pi) > 10$ and DLL$(p-K) < 3$ is required in order to ensure that the selected kaon canditades are indeed true kaons.

[6] χ^2 is a quantity that describes the goodness of fit of a model used to describe a set of observables. A good description is characterized by $\chi^2 = ndf$ where ndf is the number of degrees of freedom. $\chi^2/ndf >> 1$ indicates a bad description and is thus cut away.

Table 4.2: Selection requirements for the data sample used in the analysis

Quantity	Requirement
all tracks χ^2/ndf	< 4
muon DLL$(\mu - \pi)$	> 0
p_t of muon	> 500 MeV/c
J/ψ vertex χ^2/ndf	< 11
J/ψ mass window	-48 to $+43$ MeV/c^2
K χ^2_{IP}	> 9
K RICH PID	DLL$(K - \pi) > 10$ & DLL$(p - K) < 3$
Sum p_t of K^+ and K^-	> 900MeV/c
K^+K^- vertex χ^2/ndf	< 10
K^+K^- mass window	$990 - 2230$ MeV/c^2
B^0_s mass window	$5160 - 5580$ MeV/c^2
B^0_s χ^2_{IP}	< 25
B^0_s flight distance	> 1.5mm
B^0_s vertex χ^2/ndf	< 5
B^0_s pointing, $cos\theta_p$	> 0.99993

4.3 Analysis Data Sample

As a first check whether a clean $B^0_s \to J/\psi K^+K^-$ data sample was selected the mass distributions of the B^0_s candidates and the combined K^+K^- are reviewed.

The masses of the B^0_s candidates, $m(J/\psi K^+K^-)$, (or the di-kaon systems) can be calculated from the four-momenta of the decay products using momentum conservation. For example, for the decay $B^0_s \to J/\psi\phi$ with the ϕ momentum P_ϕ and the J/ψ momentum $P_{J/\psi}$[7] the mass of the B^0_s, $m(B^0_s)$, is given by[8]:

$$m(B^0_s)^2 = P^\mu_{B^0_s} P_{B^0_s \mu} = (P^\mu_{J/\psi} + P^\mu_\phi)(P_{J/\psi\mu} + P_{\phi\mu}) \ . \tag{4.1}$$

As explained in Section 2.1 the precise value of $m(B^0_s)$ can vary within a characteristic width because of the finite hadron lifetime. This is what makes looking at mass distributions, i.e., the masses calculated for many events, so interesting. If the decay products really come from a common particle and do not just have crossing paths, this should be visible as a peak in the distribution of the invariant mass.

A histogram of the masses of the selected B^0_s candidates, i.e., the invariant masses of the $J/\psi(\mu^+\mu^-)K^+K^-$ system, is shown in Figure 4.1. Indeed a clear signal peak is visible at the B^0_s mass indicating the presence of a B^0_s meson. In addition there is

[7] It should be noted that also the ϕ and J/ψ momentum cannot be measured directly but have to be calculated from their decay products and so forth.

[8] Note: Einstein notation is used and c=1.

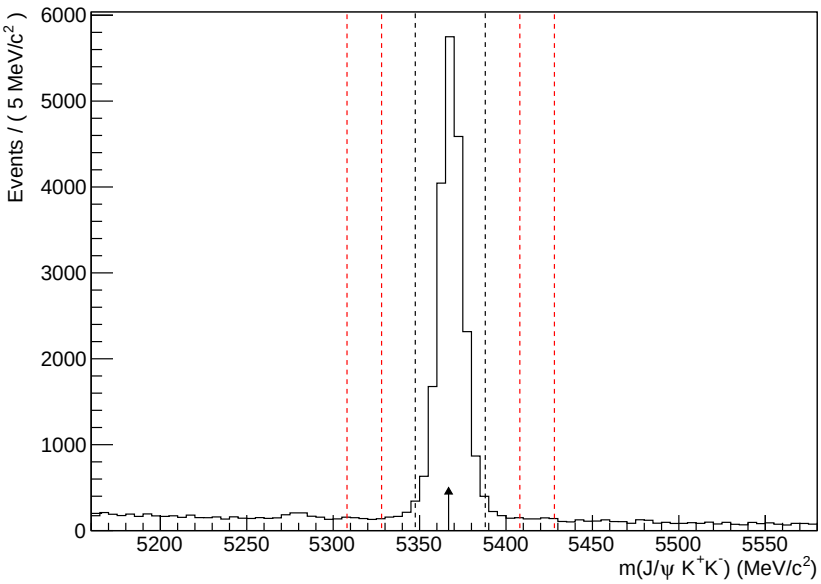

Figure 4.1: Invariant mass distribution of the $B_s^0(J/\psi K^+K^-)$ candidates. Events from the signal region marked by the two dashed black lines and the sideband regions between the red dashed lines are used to create the histograms in Fiugre 4.2. The black arrow at 5366.77 MeV/c^2 indicates the PDG value of the B_s^0 mass.

some underlying background. Since there is no other visible structure in the mass distribution it is assumed that the background is purely combinatorial. This means that some randomly selected kaons and muons were accidentally reconstructed as a B_s^0 without really originating from one. As a consequence their masses do not peak in the true B_s^0 mass but have a flat, random distribution. In addition also real decays can be misidentified as $B_s^0 \to J/\psi K^+K^-$ if they are very similar. It's quite possible that the small peak below 5300 MeV/c^2 originates from such events. However, this was not investigated in this thesis.

The distribution of the invariant masses of the two kaons in the B_s^0 signal region is shown by the black histogram in Figure 4.2. Only events with a B_s^0 candidate's mass between $\pm$20 MeV/c^2 of the B_s^0 mass are considered. There are two clearly visible peaks at $\sim$1020 MeV/c^2 and $\sim$1525 MeV/c^2 in the mass distribution. The left peak corresponds to the decay $B_s^0 \to J/\psi\phi$ where the ϕ meson decays into K^+K^-, whereas the right one corresponds to the $f_2'(1525)$ resonance. The small mass peak above 1700 MeV/c^2 might be due to another resonance but this was not investigated in this thesis. The red histogram in Figure 4.2 is an approximation of what the combinatorial background in the mass distribution should look like. It was created from events in the m(B_s^0) sidebands, that is the B_s^0 candidates ought to have a mass between $\pm$40 MeV/c^2 and $\pm$60 MeV/c^2 of the mass peak. Here, the assumption was made that in the sidebands there are no signal events left and

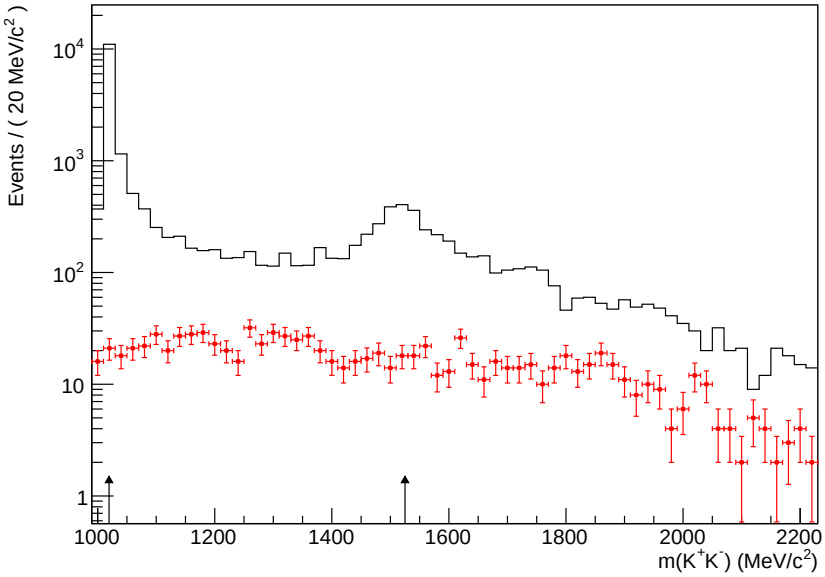

Figure 4.2: Invariant mass distribution of the combined K^+K^-. The black histogram is created from events in the B_s^0 signal region. The red dots correspond to events in the B_s^0 sidebands an thus represent combinatorial background. The peaks come from the ϕ meson and $f_2'(1525)$ resonance whose PDG masses are marked by the two black arrows at 1019.455 MeV/c^2 and 1525 MeV/c^2.

that the combinatorial background in the signal region is of the same shape as the background in the sidebands. Comparing both histograms it becomes obvious that the resonance peaks do not arise directly from the combinatorial background. The remaining part of the signal events is assumed to come from direct, non-resonant $B_s^0 \to J/\psi K^+K^-$ decays which are known to also exist [5].

4.4 Simulated Data Sample

In high energy physics simulating the experiment of interest has proven to be a very powerful tool to check the reliability of analysis methods or make any kind of physical predictions. In this thesis data created with the Monte-Carlo (MC) method [19] by the PYTHIA [20] event generator is used. It simulates both the particles emerging from proton proton collisions and their interaction with the detector. By applying the same reconstruction algorithms used in the real experiment, data sets of simulated events similar to those of the real measuring data can be created. In addition to the information on the reconstructed event signatures those MC samples, as they will be referred to, also provide information on the generator level. In that way the discrepancy between what is seen and what has really been simulated can be studied. In this thesis MC simulation is used to determine efficiencies of the LHCb detector needed for the branching ratio measurement. The procedure is discussed

in Section 6.

Used MC Samples

In order to estimate the efficiencies for the decays $B_s^0 \to J/\psi f_2'$ and $B_s^0 \to J/\psi\phi$ simulations for both types of event are necessary. Unfortunately however, there only was a $B_s^0 \to J/\psi\phi$ Monte-Carlo available at the time this analysis was done. To solve this problem, a MC for non-resonant $B_s^0 \to J/\psi K^+K^-$ decays was used to determine the values that can be expected for the f_2' efficiency. Further details are given in Section 6.

Figure 4.3 shows the mass distributions of the B_s^0 mesons and the combined K^+K^- system in both MC samples. By accessing the MC truth information, i.e., checking that an event was reconstructed as the event that was truly simulated, it was made sure that only true $B_s^0 \to J/\psi K^+K^-$ decays are considered. The missing background in the distributions is a consequence of that procedure. In the m(K^+K^-) distribution of the non-resonant Monte-Carlo no resonance peaks are visible as expected.

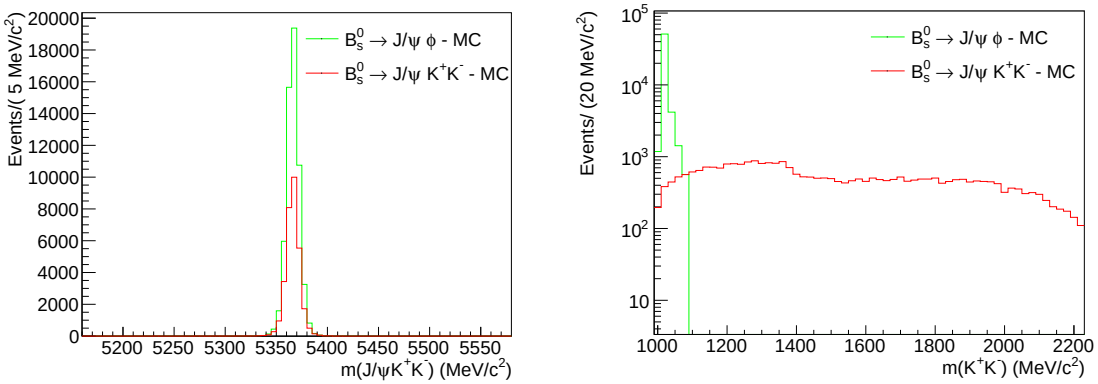

Figure 4.3: (left) Mass distribution of the true $B_s^0(J/\psi K^+K^-)$ for both MC samples. Hence, no background structure is present. The red histogram corresponds to the non-resonant $B_s^0 \to J/\psi K^+K^-$ MC, whereas the green one corresponds to the simulation of the $B_s^0 \to J/\psi\phi$ decay. (right) Corresponding distributions of the combined K^+K^- masses. The smoothness of the red distribution of the non-resonant MC sample indicates the expected absence of resonances. The clear peak in the green histogram corresponds to the ϕ resonance.

5 Analysis

For this analysis the relative branching fraction of the decay $B_s^0 \to J/\psi f_2'$ with respect to $B_s^0 \to J/\psi\phi$ is measured. For a particle that can decay by several modes,

the branching fraction $\mathcal{B}$ of one mode is the number of decays by this mode divided by the total number of decays. For the upper decays $\mathcal{B}$ can be expressed by Equation (5.1). Naturally, it has to be taken into account that only the final states $J/\psi \to \mu^+\mu^-$ and $X \to K^+K^-$[9] are considered.

$$\mathcal{B}(B_s^0 \to J/\psi X) = \frac{N_X/\epsilon_X}{2 \cdot \int \mathcal{L}\, dt \cdot \sigma_{b\bar{b}} \cdot f_{B_s^0} \cdot \mathcal{B}(J/\psi \to \mu^+\mu^-) \cdot \mathcal{B}(X \to K^+K^-)} \quad (5.1)$$

Here, N_X describes the measured number of B_s^0 decays by either the $f_2'(1525)$ or the ϕ channel in the data sample. ϵ_X is the according efficiency accounting for event losses. The subscript X takes into account that the efficiency can be a priori different for both decay modes. $\int \mathcal{L}\, dt$ is the time integrated luminosity the data corresponds to. Multiplied with the production cross section $\sigma_{b\bar{b}}$ it gives the total number of produced b and $\bar{b}$ quarks. The fraction $f_{B_s^0}$ defines how many of those are actually used for making a B_s^0 meson. The factor 2 takes into account that always a $b\bar{b}$ pair is produced and either of the quarks can be used to create a B_s^0 ($\bar{B}_s^0$) meson. The final state is considered via the explicit branching fractions $\mathcal{B}(X \to K^+K^-)$ and $\mathcal{B}(J/\psi \to \mu^+\mu^-)$.

Equation (5.1) depends on many quantities that have to be measured explicitly in order to determine the branching fraction. Unfortunately, the luminosity is not known precisely for the LHCb experiment (5%...10% uncertainty) so that it would contribute a large error. In addition, the efficiency cannot be measured using real data but has to be estimated in some other way. Consequently, it also has a large uncertainty. However, if the relative branching fraction of two decay modes is measured the luminosity cancels out because it is the same for both. Also, the relative branching fraction only depends on the ratio of efficiencies. It can be assumed that some of the uncertainties cancel out there as well. That's why such a measurement is much easier to do and provides smaller errors. Since the two considered decays are very similar further factors cancel out in the ratio. What remains can be seen in Equation (5.2):

$$\mathcal{R}_{f_2'/\phi} = \frac{\mathcal{B}(B_s^0 \to J/\psi f_2')}{\mathcal{B}(B_s^0 \to J/\psi\phi)} = \frac{N_{f_2'}}{N_\phi} \cdot \frac{\epsilon_\phi}{\epsilon_{f_2'}} \cdot \frac{\mathcal{B}(\phi \to K^+K^-)}{\mathcal{B}(f_2' \to K^+K^-)}\,. \quad (5.2)$$

In order to determine $\mathcal{R}_{f_2'/\phi}$ the event yields for the $B_s^0 \to J/\psi f_2'$ mode, $N_{f_2'}$, and for the $B_s^0 \to J/\psi\phi$ mode, N_ϕ, have to be measured. The measurement procedure will be discussed in this section. The necessary ratio of efficiencies, $\epsilon_\phi/\epsilon_{f_2'}$, is calculated using the simulated data presented in Section 4.4. Details are given in Section 6. For the explicit branching fractions $\mathcal{B}(f_2' \to K^+K^-)$ and $\mathcal{B}(\phi \to K^+K^-)$ the values from the Particle Data Group (PDG) [11] will be used.

5.1 Measurement of $f_2'(1525)$ and ϕ Yields

In order to measure how many $f_2'(1525)$- and ϕ-mesons are in the data sample they somehow have to be characterized. The easiest way to characterize a particle

[9] $X = f_2'$ or $X = \phi$

is by its mass. However, when doing this one has to keep in mind three things: First, a particle's mass is not uniquely defined but can vary within its natural width. Secondly, when measuring masses the result is limited by the resolution of the detector. Thirdly, the data sample usually is not clean but background beneath the signal distributions has to be considered. In this analysis namely combinatorial background and background from non-resonant $B_s^0 \to J/\psi K^+K^-$ play a role, as was discussed in Section 4.3

Fitting Procedure

The yields of $f_2'(1525)$ and ϕ events are determined by fitting the invariant mass distributions of the combined kaons and the B_s^0 candidates simultaneously in a two-dimensional, unbinned maximum-likelihood fit (see also Section 2.2). The fitting procedure is described in the following paragraphs, whereas the fit results will be discussed further below.

The chosen two-dimensional fit of m(K^+K^-) and m(B_s^0) has the advantage that also the background due to non-resonant decays can be fitted. It peaks in the B_s^0 mass and thus could not be distinguished from the resonant decays if only the distribution of the B_s^0 candidates' masses was considered. However, if also the m(K^+K^-) distribution is fitted the fraction of non-resonant decays can be obtained because they peak neither in the $f_2'(1525)$ nor in the ϕ mass.

The 2 dimensional pdf given in Equation (5.3) is used to describe the measured m(K^+K^-) and m(B_s^0) distributions. It is a function of m_B, which represents the B_s^0 candidates mass, and of m_{KK}, which represents the mass of the di-kaon system. It depends on a set of parameters denoted with $\vec{\lambda}$. For both $f_2'(1525)$ and ϕ the same pdf with different parameters is used.

$$\begin{aligned}\mathcal{P}_X^{tot}(m_B, m_{KK}; \vec{\lambda}) \;=\; & f_{sig} \cdot \mathcal{S}_B(m_B; \vec{\lambda}) \cdot \mathcal{S}_X(m_{KK}; \vec{\lambda}) \\ & + (1 - f_{sig}) \cdot [f_{bkg} \cdot \mathcal{BG}_B^{KK}(m_B; \vec{\lambda}) \cdot \mathcal{BG}_X^{KK}(m_{KK}; \vec{\lambda}) \\ & + (1 - f_{bgk}) \cdot \mathcal{CBG}_B(m_B; \vec{\lambda}) \cdot \mathcal{CBG}_X(m_{KK}; \vec{\lambda})]\end{aligned} \tag{5.3}$$

$\mathcal{P}_X^{tot}(m_B, m_{KK}; \vec{\lambda})$ is built from three products of individually normalized, 1-dimensional pdfs:

- $\mathcal{S}_B(m_B; \vec{\lambda})$ and $\mathcal{S}_X(m_{KK}; \vec{\lambda})$ describe the signal parts of the mass distributions,
- $\mathcal{BG}_B^{KK}(m_B; \vec{\lambda})$ and $\mathcal{BG}_X^{KK}(m_{KK}; \vec{\lambda})$ the background due to non-resonant decays, and
- $\mathcal{CBG}_B(m_B; \vec{\lambda})$ and $\mathcal{CBG}_X(m_{KK}; \vec{\lambda})$ the combinatorial background.

The signal fraction, f_{sig}, and the fraction of the first background component with respect to the total background, f_{bkg} have to be between 0 and 1 to assure that also the total pdf is normalized, that is

$$\int \mathcal{P}_X^{tot}(m_B, m_{KK}; \vec{\lambda})\, dm_B\, dm_{KK} = 1$$

for all $\vec{\lambda}$.

For the individual pdfs the following shapes are used: In Section 2.1 it was discussed that resonances are well described by a relativistic Breit-Wigner function. However, the B_s^0 mass peak is very slim and instead of having a physical shape the visible signal peak is dominated by the detector resolution. A double Gaussian function was chosen for $\mathcal{S}_B(m_B;\vec{\lambda})$ because it describes the resolution well. The correspondent formula as well as the parameterizations of the following shapes are given in Section 2.2. The two peaks in the invariant $\mathrm{m}(K^+K^-)$ distribution are wider and detector effects do not influence their shape. That's why $\mathcal{S}_X(m_{KK};\vec{\lambda})$ has indeed the shape of a relativistic Breit-Wigner function. In case of fitting the $f_2'(1525)$ mass peak the spin-2 version is chosen, in case of the ϕ mass peak the spin-1 version according to the physical properties of the particles [11].

The kaons in the non-resonant background come from a true B_s^0. Consequently $\mathcal{BG}_B^{KK}(m_B;\vec{\lambda})$ has the same shape as $\mathcal{S}_B(m_B;\vec{\lambda})$: It is a double Gaussian function with identical parameters. To choose the shape of the according pdf for the K^+K^- mass distribution is not as trivial because the two background components superimpose each other. In the end, a second order polynomial was chosen for $\mathcal{BG}_X^{KK}(m_{KK};\vec{\lambda})$. Using real data, it is not possible to motivate this choice. It is, however, justified by the simulation of the non-resonant decay $B_s^0 \to J/\psi K^+K^-$: In the mass ranges of interest the $\mathrm{m}(K^+K^-)$ distribution in the $B_s^0 \to J/\psi K^+K^-$ MC sample can be described by a polynomial as can be seen from Figure 4.3.

It was already said that the combinatorial background component is built up from falsely reconstructed events. The lower the momenta of the contributing particles the higher the probability that an event is mis-reconstructed. That's why particles in mis-reconstructed events tend to have a lower invariant mass. The according distributions decline towards higher mass regions. Usually the background is fitted with an exponential or a polynomial with negative slope. Here, $\mathcal{CBG}_B(m_B;\vec{\lambda})$ is chosen to be a linear function. Looking at the $\mathrm{m}(K^+K^-)$ distribution of events from the B_s^0 sidebands in Figure 4.2, it seems reasonable to make $\mathcal{CBG}_X(m_{KK};\vec{\lambda})$ a second order polynomial.

To determine the event yields the pdf from Equation 5.2 is extended. That is, it is multiplied by a factor N_{ev} describing the number of events which is also fitted[10]:

$$\mathcal{P}_X^{tot}(m_B, m_{KK};\vec{\lambda}) \to N_{ev} \cdot \mathcal{P}_X^{tot}(m_B, m_{KK};\vec{\lambda}) \ . \tag{5.4}$$

In order to measure the numbers of both decays $B_s^0 \to J/\psi f_2'$ and $B_s^0 \to J/\psi\phi$ two two-dimensional fits are performed in the two mass windows around the $f_2'(1252)$ and ϕ resonance. For the f_2'-fit only events with $m_{KK} \in [1250, 2000]$ MeV/c^2 are used, for the ϕ-fit only such with $m_{KK} \in [1000, 1050]$ MeV/c^2. In addition the fits are limited to $m_B \in [5290, 5450]$ MeV/c^2

The pdf has one weak spot that has to be born in mind: There is no way for the fitter to distinguish between the combinatorial and non-resonant background in the

[10]This procedure is known as an extended maximum-likelihood fit. [21]

combined K^+K^- mass because they have similar shapes. To solve this problem, first $\mathcal{CBG}_X(m_{KK};\vec{\lambda})$ is fitted independently to events from the B_s^0-sidebands, i.e., the combinatorial background. Then the parameters of the polynomial are kept fixed in the actual 2-dimensional fit.

Fit Results

The outcome of the two-dimensional fits can be used to calculate the event yields. Before this is done at the end of this section it is necessary to evaluate the fit results. Inconveniently, there is no direct way to quantify the quality of a maximum-likelihood fit. In the case of a an unbinned and two-dimensional fit it is not even possible to evaluate graphically whether the pdf describes the fitted data well. To still evaluate the quality of the fit result, the (binned) mass histograms are compared to the one-dimensional projections of the pdf. The projection on m_{KK} is given by:

$$\mathcal{P}_X(m_{KK};\vec{\lambda}) = \int_{m_{B\,min}}^{m_{B\,max}} \mathcal{P}_X(m_{KK}, m_B;\vec{\lambda}) dm_B \ , \tag{5.5}$$

the one on m_B can be defined accordingly. However, even if the data is described well in one dimension, this does not necessarily have to imply a good fit in two dimensions.

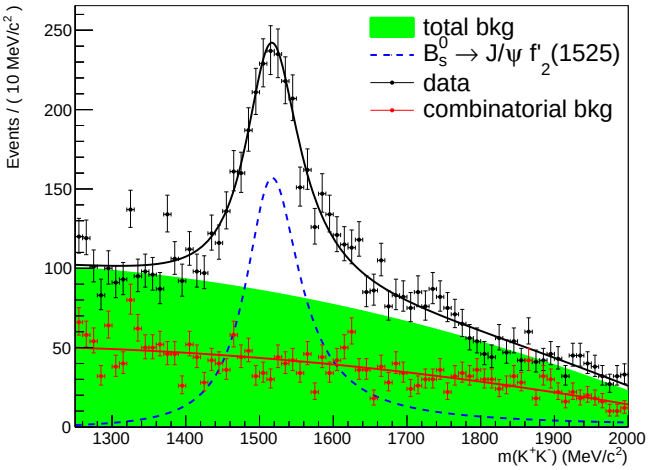

Figure 5.1: Invariant mass of the combined K^+K^- and fit in the $f_2'(1525)$ mass window. The black line shows the projection of the total pdf on m_{KK}, the blue, dashed line its signal part and the green area the total background. The red data points and line represent the combinatorial background and the part of the pdf describing it.

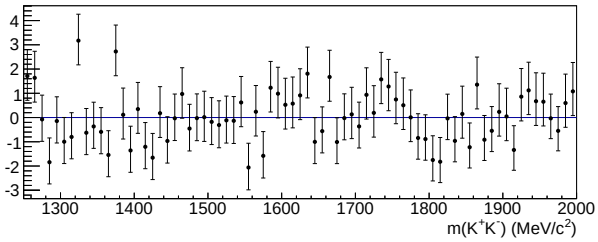

Figure 5.2: Pull distribution of the K^+K^- mass histogram and the fitted pdf shown in Figure 5.1.

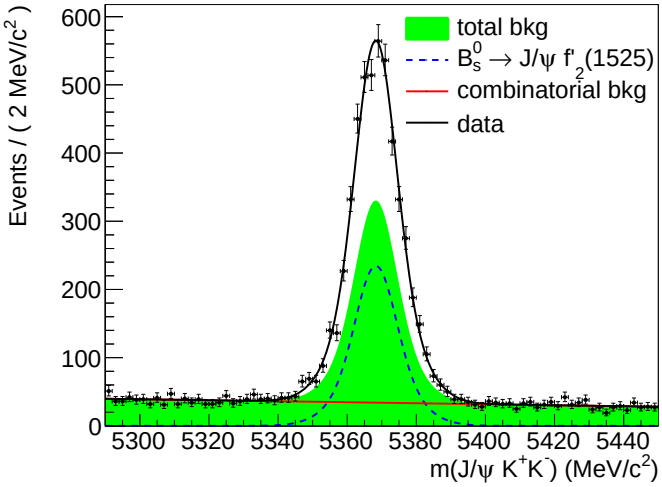

Figure 5.3: Invariant mass of the B_s^0 candidate and fit in the $f_2'(1525)$ mass window. The black line shows the projection of the total pdf on m_B, the blue, dashed line its signal part, the red line the part describing the combinatorial background and the green area the total background including non-resonant $B_s^0 \to J/\psi K^+K^-$ decays.

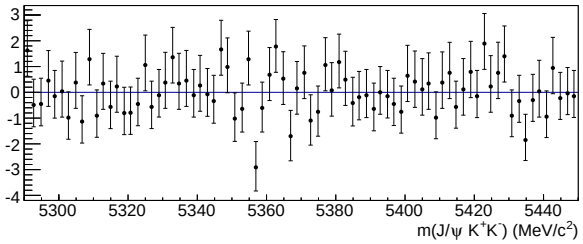

Figure 5.4: Pull distribution of the $J/\psi K^+K^-$ invariant mass histogram and the pdf projection shown in Figure 5.3.

The distribution of the invariant K^+K^- mass in the f_2' mass window is shown in Figure 5.1. In addition also the projection of the fitted pdf is plotted. For visualization the pdf is split up in its individual components. It might be helpful to keep in mind that the histogram in Figure 5.1 corresponds to Figure 4.2. Naturally, only the mass range of the $f_2'(1525)$ resonance, i.e., the right mass peak in Figure 4.2, is shown.

To be able to compare the mass histogram and the pdf better, the bin-wise pull distribution is given in Figure 5.2. The pull of the i-th bin is defined as the difference between the pdf value for the bin and the histogram entry divided by the statistical error of the latter:

$$\frac{h(m_i) - \mathcal{P}(m_i; \vec{\lambda})}{\Delta h(m_i)}. \tag{5.6}$$

If the pull distribution is distributed symmetrically around 0 according to a Gaussian function with width 1 this is evidence for agreement within the errors.

Except for some spikes the data points in the f_2' mass histogram are described well by the pdf projection. However, there seems to be a small signal peak slightly above 1700 MeV/c^2 that is not considered by the pdf. As was already assumed in Section 4.3 this could be evidence for another resonance. In the PDG [11] the $f_0(1710)$ is listed with a mass of 1720 ± 6 MeV/c^2 and a width of 135 ± 8 MeV/c^2. It is known to decay into two opposite sign kaons but the decay $B_s^0 \to J/\psi f_0(1710)$

has not been observed. In Section 5.3 the fit is redone allowing for the presence of a $f_0(1710)$ resonance peak. The result will be used to estimate a systematic error.

Figure 5.3 shows the B_s^0 candidate's mass distribution for events with m(K^+K^-) in the f_2' mass window as well as the pdf projection. The corresponding pull distribution in the m_B dimension can be seen in Figure 5.4. Neither of the figures indicate a systematic discrepancy but they rather show a good agreement between the pdf and the data points.

The projections of the pdf from the fit in the ϕ mass window are shown in Figure 5.5 and Figure 5.7 together with the mass histograms. Again, the histogram in Figure 5.5 corresponds to Figure 4.2 but shows the left mass peak only. The mass plots as well as the pull distributions given in Figure 5.6 and 5.8 suggest a good description of the one-dimensional distributions by the pdf. In comparison to the f_2' fit the very low background in the ϕ region is noteworthy.

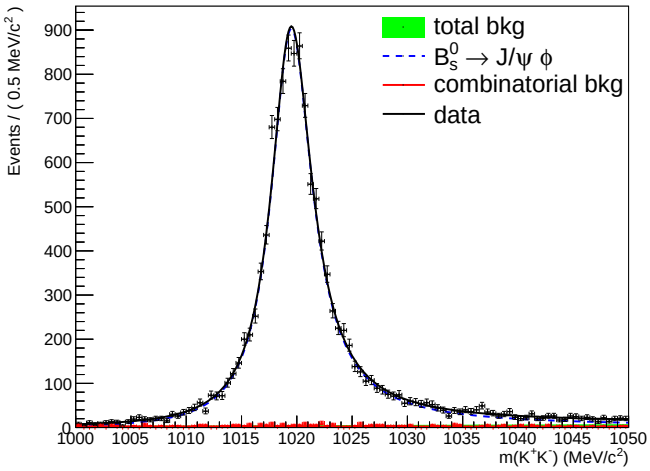

Figure 5.5: Invariant mass of the combined K^+K^- and fit in the ϕ mass window. The black line shows the projection of the total pdf on m_{KK}, the blue, dashed line its signal part and the green area the background. The red data points and line represent the combinatorial background and the part of the pdf describing it.

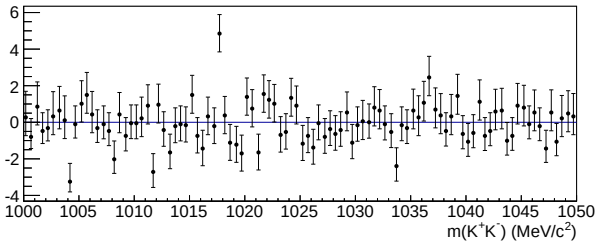

Figure 5.6: Pull distribution of the combined K^+K^- mass histogram in Figure 5.5 and the pdf projection of the fit in the ϕ mass window.

Some of the fit parameters for both fits are summarized in Table 5.1. The total number of events, including signal and both background components, and the signal fraction are of special interest because the $f_2'(1525)$ and ϕ yields can be calculated from them. In addition, some physical parameters of the signal peaks are given even if it is no goal of this thesis to measure them.

The measured mass values are fairly close to the values given by the PDG. Indeed, some of the deviations are larger than 3σ but it also has to be assumed that the errors

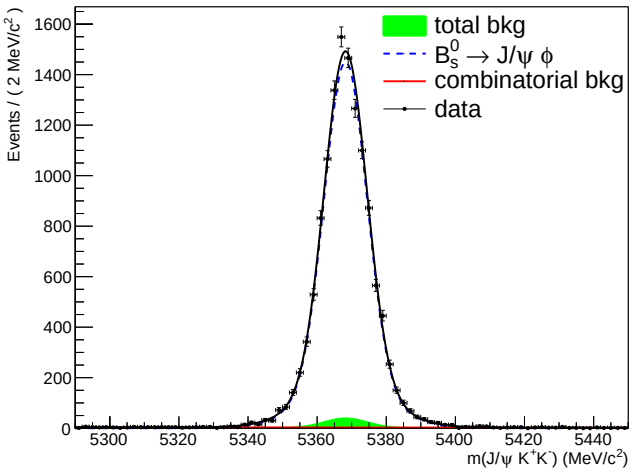

Figure 5.7: Invariant mass of the B_s^0 candidate and fit in the ϕ mass window. The black line shows the projection of the total pdf on m_B, the blue, dashed line its signal part, the red line the part describing the combinatorial background and the green area the total background including non-resonant $B_s^0 \to J/\psi K^+K^-$ decays.

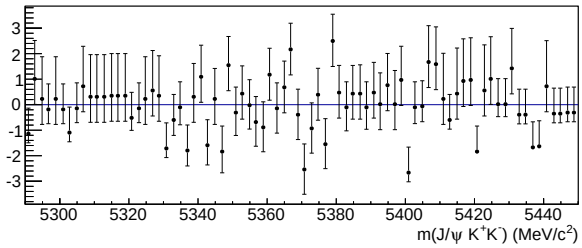

Figure 5.8: Pull distribution of the $J/\psi K^+K^-$ mass histogram in Figure 5.7 and the according pdf projection.

determined by the fit are too small. That is because some systematic effects that would increase them were ignored. First of all, it was not systematically analyzed whether the double Gaussian function that was chosen to describes the B_s^0 signal peak really provides the accurate shape. Secondly, there is still some final calibration of the 2011 data to be done. Due to inaccuracies in the detector alignment particle momenta are not calculated correctly, which also affects mass spectra.

Table 5.1: Some fit parameter values with physical meaning for the two fits in the $f_2'(1525)$ and the ϕ mass window. Also, the corresponding PDG values are given [11].

Parameter	$f_2'(1525)$-Fit Value	ϕ-Fit Value
N_{ev}	7353 ± 86	12875 ± 113
f_{sig}	27.87 ± 1.38 %	95.69 ± 0.06 %
f_{bkg}	48.85 ± 1.32 %	60.79 ± 6.24 %
m_X	1520.90 ± 1.87 MeV/c^2	1019.60 ± 0.03 MeV/c^2
Γ_X	90.93 ± 6.19 MeV/c^2	4.60 ± 0.07 MeV/c^2
$m_{B_s^0}$	5368.30 ± 0.13 MeV/c^2	5368.20 ± 0.06 MeV/c^2
PDG m_X	1525 ± 5 MeV/c^2	1019.455 ± 0.020 MeV/c^2
PDG Γ_X	73^{+6}_{-5} MeV/c^2	4.26 ± 0.04MeV/c^2
PDG $m_{B_s^0}$	5366.77 ± 0.24 MeV/c^2	

What is more severe, is the discrepancy of the $f_2'(1525)$ widths. It seems to be larger

than can be explained by the expected precision of the measurements. One possible explanation could be that the Breit-Wigner signal pdf is widened by the observed mass peak above the $f_2'(1525)$ resonance in the m(K^+K^-) distribution. This will be further analyzed in Section 5.3.

The number of $B_s^0 \to J/\psi f_2'(1525)$, $N_{f_2'}$, and $B_s^0 \to J/\psi\phi$ decays, N_ϕ, can now be calculated from the total numbers of events, N_{ev}, and the signal fractions, f_{sig}, obtained from the two fits.

$$N_X = N_{ev} \cdot f_{sig} \pm \sqrt{(\Delta N_{ev} f_{sig})^2 + (N_{ev} \Delta f_{sig})^2} \tag{5.7}$$

It has yet to be considered that the pdfs are normalized over the fitted mass ranges only. Consequently, $N_X \cdot f_{sig}$ is the number of signal events in those ranges. Looking at Figure 5.1 and 5.5 it becomes obvious that there are also some signal events outside of the f_2' and ϕ mass windows. There's a significant part of the signal pdf crossing the borders of the m_{KK} range. Integrating the signal part of the pdf from Equation (5.3) reveals that there are 93.70% of the total integral in the f_2' mass window and 91.12% in the ϕ mass window. Considering this it is found that $N_{f_2'} = 2187 \pm 111$ and $N_\phi = 13519 \pm 149$. The corresponding ratio is: $N_{f_2'}/N_\phi = (16.18 \pm 0.84)\%$.

5.2 Validation of the Fitting Procedure

In addition to the graphical evaluation of the fit results that was discussed in the previous section it is also necessary to check the quality of the parameter values. This can be done via a toy study where it is tested how well the fitting algorithm determines the fit parameters and their errors. In the toy study that was performed for this analysis the pdf $\mathcal{P}_X^{tot}(m_B, m_{KK}; \vec{\lambda})$ from Equation (5.3) was used to create 500 data samples. In order to provide enough statistics each sample consisted of approximately $100,000$ B_s^0 candidates; the exact number of events fluctuated randomly. The pdf was then fitted to the generated m_{KK} and m_B distributions in an extended maximum-likelihood fit according to the fitting procedure discussed in Section 5.1. The results of the 500 fits can be used to check whether the fit parameters and their errors are determined well or whether there is some bias. This is done by looking at the pull distributions of the parameters. Similarly to the definition above, the pull distribution of a fit parameter λ is defined via the difference of the original value used in the generation of the sample and the fitted value divided by the error of the latter:

$$p(\lambda) = \frac{\lambda_{gen} - \lambda_{fit}}{\Delta\lambda_{fit}} \ . \tag{5.8}$$

For a proper fitting algorithm $p(\lambda)$ should be distributed according to a Gaussian with mean $\mu = 0$ and width $\sigma = 1$.

The pull distributions of the free fit parameters can be seen in Figure 5.9. They are each fitted with a Gaussian function whose μ and σ are also displayed in the figure.

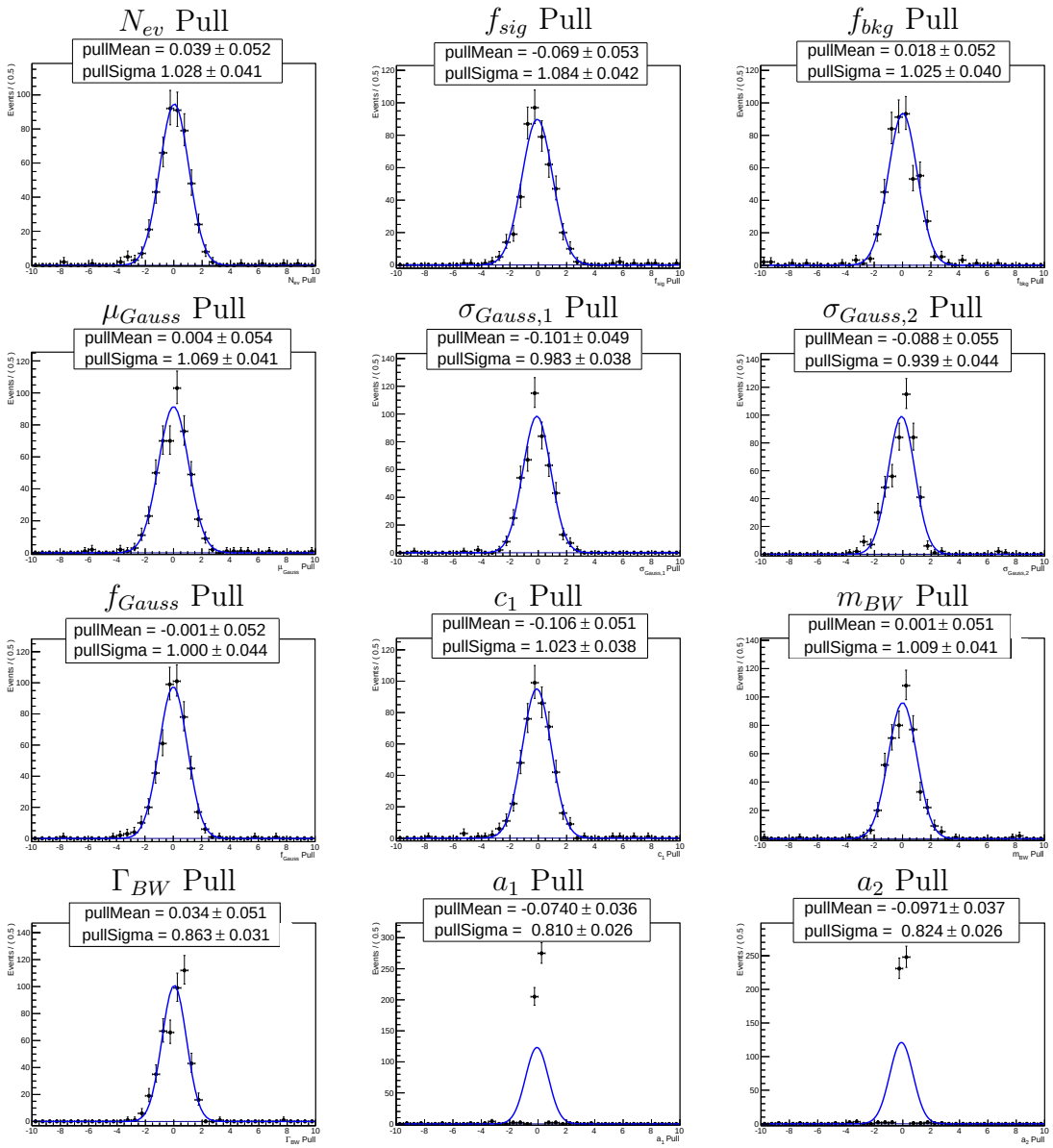

Figure 5.9: Pull distributions of the free fit parameters resulting from the toy study. Each distribution is fitted with a gaussian function whose mean and width are given in in the plots.

Most of the parameters do indeed meet the requirements and provide $\mu = 0$ and $\sigma = 1$ within the errors. Only the distributions for a_1 and a_2, i.e., the parameters of the free background component $\mathcal{BG}_X^{KK}(m_{KK}; \vec{\lambda})$, are much slimmer than anticipated. This indicates that the parameter errors are determined too large. However, since the parameters are not used in the further analysis this is not a serious problem and thus will be disregarded.
The toy study is taken as an indication that the fitting method works as expected and does indeed give correct results.

5.3 Fit Systematics

The parameters resulting from the fit somewhat depend on the chosen probability density function, which can also affect the measured (relative) event yields. This is a problem because some parts of the pdf, like the $m(B_s^0)$ signal shape, were chosen intuitively. Other shapes would have been possible as well and the correct choice is not known. In order to estimate the influence of the chosen shape on the results, the pdf is slightly varied and then fitted to the data distributions again. An error is estimated by looking at the change of the relative event yields. In the end, only those are relevant for the relative branching fraction. As a default value, the value measured in Section 5.1 is used.

$$\sigma = \frac{\left(N_{f_2'}/N_\phi\right)_{varied} - \left(N_{f_2'}/N_\phi\right)_{default}}{\left(N_{f_2'}/N_\phi\right)_{default}} \tag{5.9}$$

The variations of the pdf and the errors they cause are summarized in Table 5.2. The largest error is then taken as an estimate of the systematical error due to the shape of the pdf.

Table 5.2: Estimation of the systematic error due to the fit model.

Variation	$\sigma_{syst}[\%]$
fix γ of $f_2'(1525)$ to PDG value 73 MeV/c^2 and include $f_0(1710)$ resonance into pdf	-7.3
linear non-resonant m(K^+K^-) background	$+12.5$
describe m(B_s^0) with Gaussian function	$+3.1$
exponential m(B_s^0) background	-0.9
max σ_{syst}	$+12.5$ -7.3

Of special interest is the first entry in Table 5.2 where a spin-0 Breit-Wigner was added to the f_2' background pdf to allow for the presence of a second resonance peak. As a first approximation a double Gaussian was chosen for the according part of the pdf in the m(B_s^0) distribution assuming that the resonance does indeed come from a B_s^0 decay. The results of the fit, where the $f_2'(1525)$ and $f_0(1710)$ widths were fixed to the PDG values, is shown in Figure 5.10. The fit gives a $f_0(1710)$ mass of (1718 ± 9) MeV/c^2 in agreement with the PDG value of (1720 ± 6) MeV/c^2 [11]. This and the good description of the data as shown in the plots makes the existence of a $f_0(1710)$ or a similar resonance seem likely. This would be a first sign of the decay $B_s^0 \to J/\psi f_0(1710)$. Unfortunately, within this thesis it was not possible to investigate this any further.

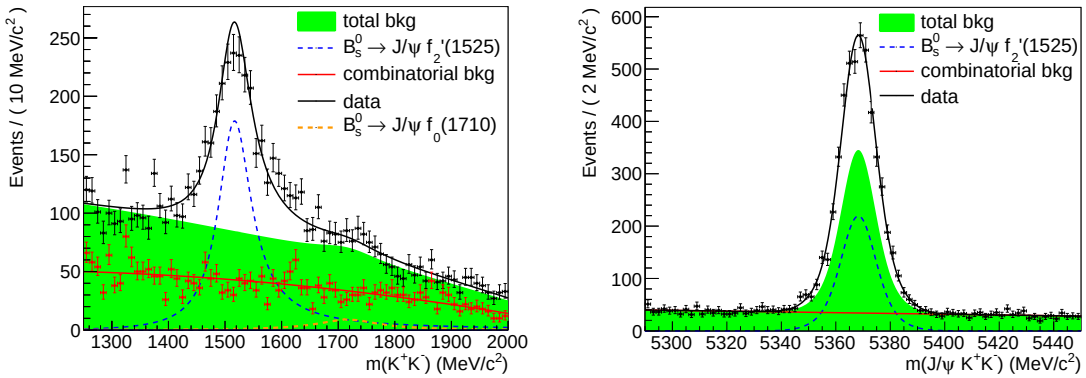

Figure 5.10: Fit in the f_2' mass window allowing for an additional $f_0(1710)$ resonance. The left plot shows the invariant K^+K^- mass distribution whereas the right one the distribution of the B_s^0 candidate's mass. The significant difference with respect to Figure 5.1 and 5.3 is that the total background, shown in green, now includes a Breit-Wigner part in m_{KK} and an additional double Gaussian in m_B. The orange dashed line shows the fitted $f_0(1710)$ resonance by itself.

6 Efficiency Corrections

The event numbers measured in Section 5 have to be corrected due to the finite efficiency of the LHCb experiment. In several stages events are lost and thus do not appear in the data sample used for the analysis. Each effect causing event losses can be assigned an efficiency. The total efficiency ϵ then is the product of all contributing efficiencies:

$$\epsilon = \epsilon_{acc} \cdot \epsilon_{rec} \cdot \epsilon_{sel} \cdot \epsilon_{trig} \ . \tag{6.1}$$

ϵ_{acc} takes into account that of the real number of decays, N_{real}, only a fraction $N_{acc} = \epsilon_{acc} \cdot N_{real}$ lies within the acceptance of the detector, i.e., within its field of vision. Even those who indeed produce signals do not have to be reconstructed properly. This gives rise to $\epsilon_{rec} = N_{rec}/N_{acc}$, where N_{rec} is the number of reconstructed events. In the selection process not only wrongly reconstructed background events are discarded by the cuts but also some signal events. The remaining fraction is given by $N_{sel} = \epsilon_{sel} \cdot N_{rec}$. Finally, also the trigger requirements lead to the rejection of some signal events which is considered by $\epsilon_{trig} = N_{trig}/N_{sel}$.

In general ϵ can depend on the specific decay, which, in the following, will be indicated by a subscript X. In this thesis X can be either f_2' or ϕ depending on which of the two decays $B_s^0 \to J/\psi f_2'$ or $B_s^0 \to J/\psi\phi$ is studied.

Using real data it is impossible to measure the discussed efficiencies. Therefore, simulated data of the non-resonant decay $B_s^0 \to J/\psi K^+K^-$, that was presented in Section 4.4, is used to estimate the efficiencies for both channels $B_s^0 \to J/\psi f_2'$ and $B_s^0 \to J/\psi\phi$. As it is not obvious that the applied method gives the right values, the

efficiency for $B_s^0 \to J/\psi\phi$ is also calculated using simulated data of the $B_s^0 \to J/\psi\phi$ decay in order to have some cross-check.

6.1 Comparison Between Fully Simulated Events and Real Data

Before a MC simulation can be used to make predictions for the real experiment it is essential to compare the simulation with data and make sure that they are compatible in the quantities of interest. As the non-resonant MC sample is to be compared to the measured data with the two resonances $f_2'(1525)$ and ϕ particular attention has to be paid to the kaon kinematics. The corresponding distributions have to agree because the total efficiency depends on them. This can be seen in Figure 6.1.

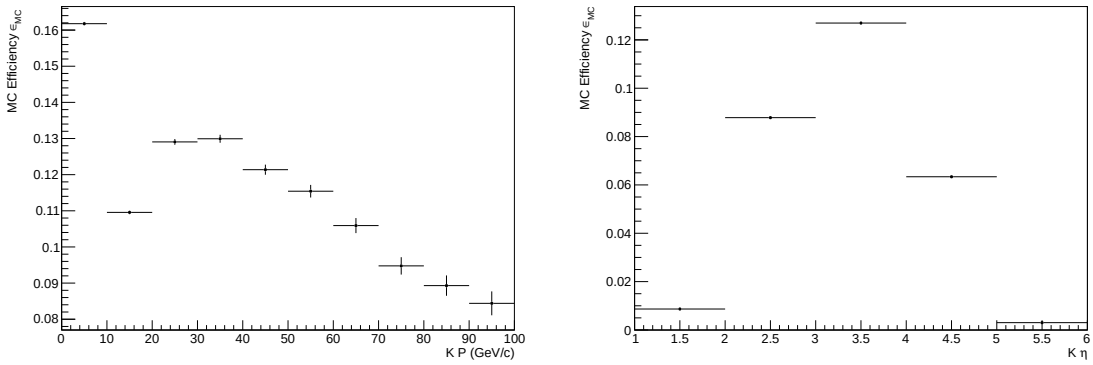

Figure 6.1: Efficiencies measured in the non-resonant $B_s^0 \to J/\psi K^+K^-$ Monte-Carlo. The left plot shows the kaon momentum dependency whereas the right one shows the dependency of ϵ_{MC} on the pseudorapidity. Further details of measuring MC efficiencies are discussed in Section 6.2.

The distributions of momentum P, transverse momentum $\mathrm{P_T}$ and pseudorapidity η[11] of the kaons in data and both MC samples are compared in Figure 6.2, 6.3 and 6.4. No difference is made between negatively and positively charged kaons because they behave alike.

The comparisons are made for the two mesons separately by looking at two different mass windows. Most $f_2'(1525)$ mesons have a mass within $[1400, 1650]$ MeV/c^2 whereas most ϕ mesons can be found in $[1000, 1050]$ MeV/c^2. Events are only taken into account if their combined K^+K^- mass lies within those windows. To make sure that only kaons from the resonances are compared, events from the m(K^+K^-) sidebands are used to correct the background contribution in the measured data. In the simulation background is avoided by only taking kaons from truthfully reconstructed events.

[11]The pseudorapidity is commonly used in particle physics to describe the angle Θ between the particle's momentum and the beam axis of the experiment: $\eta = -\,ln\left(tan\left(\frac{\Theta}{2}\right)\right)$.

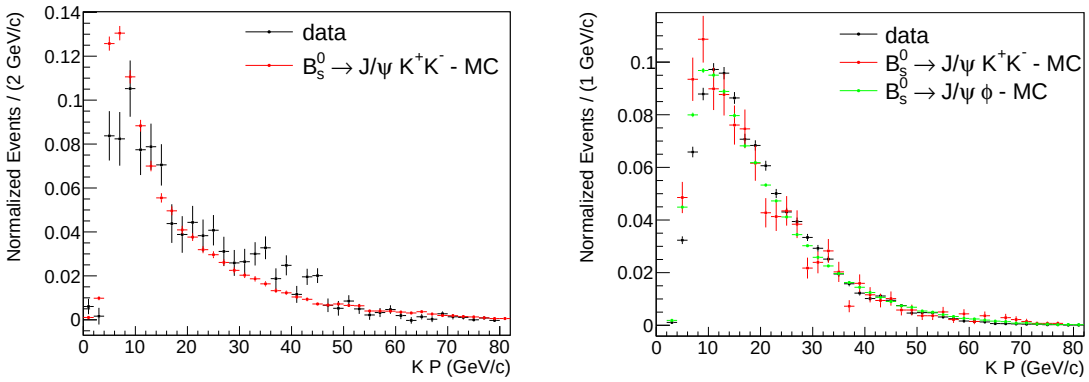

Figure 6.2: Kaon momentum P for data and both MC samples. Data is shown in black, the non-resonant $B_s^0 \to J/\psi K^+K^-$-MC in red and the $B_s^0 \to J/\psi\phi$-MC in green. The histograms are all normalized by dividing by their number of entries. In the left plot only events with m(K^+K^-) in the f_2' mass window are considered, in the right plot only such with m(K^+K^-) in the ϕ mass window.

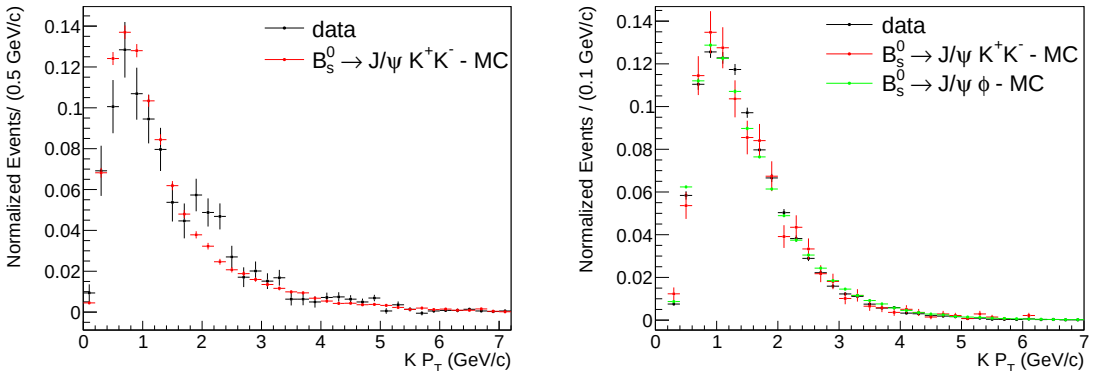

Figure 6.3: Kaon transverse momentum P_T for data and both MC samples. For a more detailed description see Figure 6.2.

In some bins of the compared distributions there are discrepancies larger than the statistical errors. Especially in the lower momentum regions the simulation does not agree with the real data. Usually, this problem could be solved by reweighing the MC distributions. However, this was found to give no considerable improvement because of the relatively good overall agreement and the low statistics in some of the distributions. Especially noteworthy is the agreement of the $B_s^0 \to J/\psi\phi$ simulation with the non-resonant $B_s^0 \to J/\psi K^+K^-$ simulation in the ϕ mass window. This shows that there is no significant difference in the kaon kinematics independent of whether there is a ϕ resonance or not. It is assumed that this is also valid for the $f_2'(1525)$ resonance.

Altogether, it seems to bee a good first approximation to determine efficiencies for the decays $B_s^0 \to J/\psi f_2'(1525)$ and $B_s^0 \to J/\psi\phi$ with the simulation of the non-

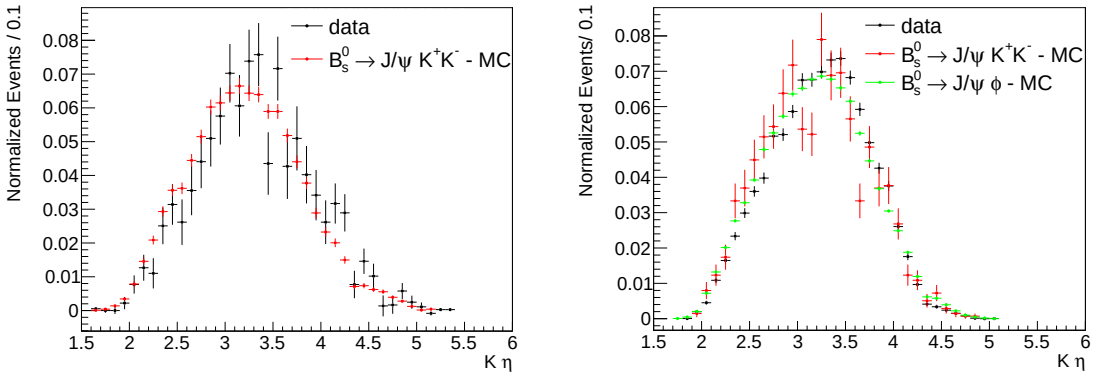

Figure 6.4: Kaon pseudorapidity η for data and both MC samples. For a more detailed description see Figure 6.2.

resonant $B_s^0 \to J/\psi K^+K^-$ decay. The efficiency measured for the $B_s^0 \to J/\psi\phi$ channel with the corresponding simulation can be used as a cross-check.

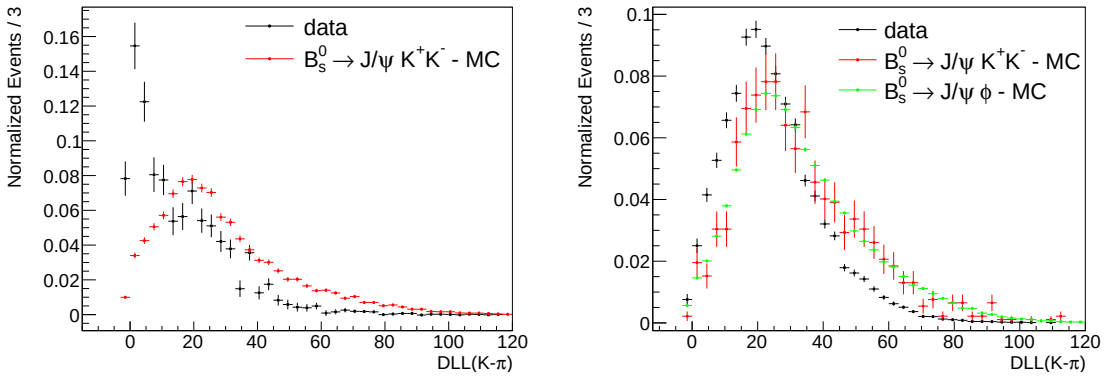

Figure 6.5: Comparison of the DLL($K-\pi$) distributions for kaons of events in the f_2' and ϕ mass window. For a more detailed description see Figure 6.2.

When comparing the measured and simulated data samples another problem can be noted: There is a significant discrepancy in the DLL($K-\pi$) and DLL($p-K$) distributions which can be seen in Figure 6.5 and 6.6. This is a problem because there are cuts on those variables in the selection which consequently have different efficiencies in measured data and MC. To avoid a systematic effect on the selection efficiency, ϵ_{sel} is split up into two parts. The first part gives the efficiency of the selection requirements without the DLL-cuts and is determined with the $B_s^0 \to J/\psi K^+K^-$-MC in Section 6.2. The second part is the efficiency of the DLL-cuts, ϵ_{DLL}, which is measured with a data driven method that is described in Section 6.3.

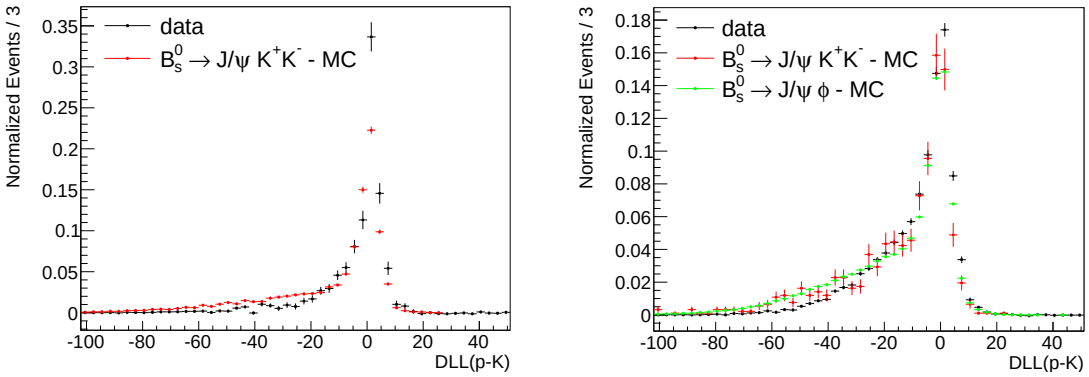

Figure 6.6: Comparison of the DLL$(p-K)$ distributions for kaons of events in the f_2' and ϕ mass window. For a more detailed description see Figure 6.2.

6.2 Monte-Carlo Efficiencies

In simulated data efficiencies can be determined very easily because the generator level information is accessible. This means that it is known what has been generated and in each step of the measuring, reconstruction and selection process it can be checked what happens with the generated events. For example, it is known whether they are reconstructed correctly or whether or not they pass a certain selection requirement. As was seen before an efficiency can be defined as the fraction of events that passes a certain criterion. In a MC data sample those events can simply be counted. The total efficiency can then be determined by counting the fraction of the total number of generated events that is reconstructed correctly and is selected in the data sample. Similarly, the acceptance efficiency can be calculated by counting the number of events that are within the detector acceptance, the reconstruction efficiency by counting the the number of reconstructed events and so on. Consequently, each of the efficiencies given in Equation (6.1) can be determined.

As was said before there was no MC sample for the decay $B_s^0 \to J/\psi f_2'(1525)$ available for this analysis. That is why the efficiencies for both decay modes $B_s^0 \to J/\psi\phi$ and $B_s^0 \to J/\psi f_2'(1525)$ are determined from the non-resonant $B_s^0 \to J/\psi K^+K^-$-MC sample. It should be mentioned again that the MC distributions are not reweighed with the data distributions. The question remains, how the two modes can be distinguished in the non-resonant MC. As a first approximation it seems reasonable to do it by the mass of the combined K^+K^-. Indeed, Figure 6.1 shows that the efficiency depends on the kinematics of the kaons but in Section 6.1 it was seen that the kinematic distributions of data and the $B_s^0 \to J/\psi K^+K^-$-MC agree for events with m(K^+K^-) in the ϕ and f_2' mass window. This is taken as a sign that the kinematic dependency of the efficiency is equivalent to a dependency on the K^+K^- mass.

The total efficiency measured in the MC sample, ϵ_{MC}, is plotted against m(K^+K^-) in Figure 6.7. It depends on m(K^+K^-) as was expected. Most ϕ mesons can be

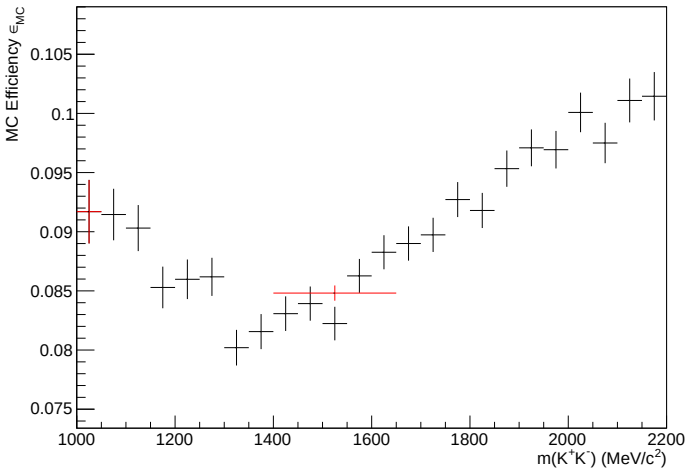

Figure 6.7: Efficiency ϵ_{MC} for the non-resonant MC sample depending on the combined K^+K^- mass. The black histogram shows the mass dependence for a fine binning. The red points are the mean values in the f_2' and ϕ mass window used for the decays $B_s^0 \to J/\psi f_2'(1525)$ and $B_s^0 \to J/\psi\phi$.

found in a relatively small mass range $m(K^+K^-) \in [1000, 1050]$ MeV/c^2. Figure 6.7 indicates that fluctuations of the efficiency values are negligible in this range. That is why the mean efficiency over the range is taken for the decay $B_s^0 \to J/\psi\phi$. For the decay $B_s^0 \to J/\psi f_2'(1525)$ the mean efficiency in the K^+K^- mass range $\mathrm{m}(K^+K^-) \in [1000, 1050]$ MeV/c^2 is used. The resulting values are listed in Table 6.1 and also shown in Figure 6.7.

Table 6.1: Efficiencies calculated from the $B_s^0 \to J/\psi K^+K^-$ Monte-Carlo sample in the $f_2'(1525)$ and ϕ mass window. All errors are statistical.

Efficiency	f_2' Window	ϕ Window
ϵ_{acc}	23.80 ± 0.12 %	24.09 ± 0.46 %
ϵ_{rec}	94.61 ± 0.59 %	95.72 ± 2.37 %
ϵ_{sel}	45.73 ± 0.37 %	49.11 ± 1.51 %
ϵ_{trig}	82.36 ± 0.81 %	80.97 ± 3.05 %
ϵ_{MC}	8.48 ± 0.06 %	9.17 ± 0.27 %

However, it is not obvious that taking the mean value also gives the correct efficiency for $B_s^0 \to J/\psi f_2'(1525)$. f_2' events can be found in a large mass range and fluctuations in the efficiency might be significant. To check this the efficiency for $B_s^0 \to J/\psi f_2'(1525)$ was also calculated by weighting the values of each K^+K^- mass bin with the fraction of $B_s^0 \to J/\psi f_2'(1525)$ signal events in this bin. The fraction can be calculated by computing the integral of the signal part $\mathcal{S}_{f_2'}(m_{KK}; \vec{\lambda})$ of the fitted pdf describing the $\mathrm{m}(K^+K^-)$ distribution[12] (see also Section 5). The efficiency is then given by:

$$\epsilon_{MC_{f_2'}} = \sum_i \int_i \mathcal{S}_{f_2'}(m_{KK}; \vec{\lambda})\, dm_{KK} \cdot \epsilon_{MC_i} \ . \tag{6.2}$$

[12]Note that $\mathcal{S}_X(m_{KK}; \vec{\lambda})$ is already normalized.

This is done over a relatively large mass range from 1250 MeV/c^2 to 2000 MeV/c^2. The resulting efficiency is $\epsilon_{MC_{f_2'}} = 8.50 \pm 0.06$ % which is compatible with the mean value considering the statistical error. Consequently, the efficiency value given in Table 6.1 can be used for the $B_s^0 \to J/\psi f_2'(1525)$ mode.

6.3 PID Efficiency

In Section 6.1 the discrepancy of the PID distributions led to the conclusion that the efficiency ϵ_{PID} of the PID cuts can not be determined with the MC sample. That is why it is necessary to measure ϵ_{PID} with a data driven method that will be discussed in this section. Usually, the identification of pions and kaons is done by RICH detectors. However, there are some special, very clean decays where particles can be identified from their kinematics alone. Those decays can be used to measure the performance of the particle identification system. In this analysis, ϵ_{PID} is measured using the tools and calibration data samples provided by the the PIDCalib Packages [22]. This data allows to study the efficiency of arbitrary DLL-cuts with the help of the mode $D^\star(2010) \to D(K^-\pi^+)\pi_s^+$. In this mode the kaon can be identified independently from the RICH information and thus the fraction of particles passing or failing the cuts of interest can be measured. ϵ_{PID} is then given by the fraction of the passing kaons with respect to the total number of kaons in the sample.

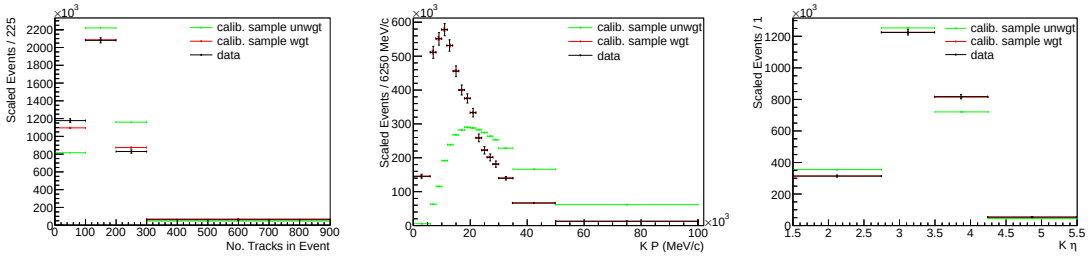

a b c

Figure 6.8: Reweighing of the calibration sample using the number of tracks per event and the two dimensional distribution of the momentum and pseudorapidity for kaons from $B_s^0 \to J/\psi\phi$. (a) shows the number of tracks, (b) the kaon momentum and (c) the pseudorapidity distributions. The green and red markers show the un-weighted and weighted distributions of the calibration sample, the black ones correspond to the analysis data sample.

However, if the result is to be transferred to other decay modes it has to be born in mind that the according DLL distributions can depend on the kinematics of the kaons. If they are different this can result in a different efficiency of the cut. That's why the calibration sample has to be reweighed with the distributions from the data sample for which the efficiency is to be measured.

The DLL distributions depend strongly on the momentum and pseudorapidity of the considered particle as well as on the number of particle tracks in the event. That

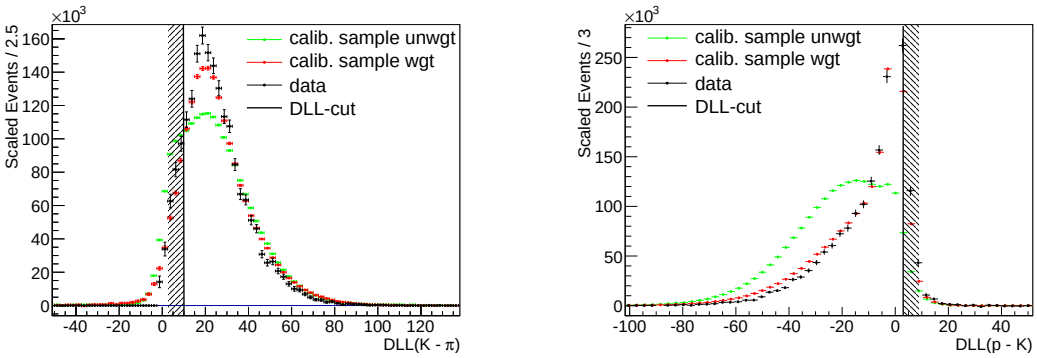

Figure 6.9: DLL($K-\pi$) (left) and DLL($p-K$) distribution (right) of the calibration sample before (green) and after the reweighing (red) with kaons from $B_s^0 \to J/\psi\phi$. The vertical lines indicate the cuts used in the selection for which ϵ_{PID} is measured.

is why first the distribution of the number of tracks in the calibration sample is reweighed according to the distribution in the analysis data sample. Then also the kaon momentum and pseudorapidity distributions are reweighed two-dimensionally. Those distributions can be seen in Figure 6.8 for the analysis and calibration data sample. The resulting DLL($K-\pi$) and DLL($p-K$) distributions are shown in Figure 6.9.

ϵ_{PID} has to be measured for both decay modes $B_s^0 \to J/\psi f_2'(1525)$ and $B_s^0 \to J/\psi\phi$. That is why it is measured with two differently reweighed calibration samples. The first sample is reweighed with the distributions of events with a K^+K^- mass in the f_2' window, the second sample with those of events from the ϕ mass window. To account for background events, which have different kinematic distributions, sideband subtraction is applied to correct the data distributions. The plots shown in Figure 6.8 and 6.9 correspond to the analysis of the $B_s^0 \to J/\psi\phi$ channel.

The resulting efficiencies of the PID cuts are given in Table 6.2 for both decay modes $B_s^0 \to J/\psi f_2'(1525)$ and $B_s^0 \to J/\psi\phi$ and will be used in the further analysis.

Table 6.2: Efficiencies of the DLL cuts in the f_2' and ϕ mass window.

Decay Mode	ϵ_{PID}
$B_s^0 \to J/\psi f_2'$	$70.79 \pm 0.76\%$
$B_s^0 \to J/\psi\phi$	$77.50 \pm 0.14\%$

6.4 Real Data Efficiencies

The measured MC efficiencies ϵ_{MC} can be used to estimate the efficiencies of the real experiment. However, they are not directly transferable because in order to save computing time only events that decay into a certain solid angle are generated in the MC simulation. Consequently, event yields in MC have to be corrected with

a geometric efficiency ϵ_{geom}. For the non-resonant $B_s^0 \to J/\psi K^+K^-$ MC sample $\epsilon_{geom} = 15.53\%$ [23]. Considering also the efficiency of the PID cuts the total efficiencies used for the decays $B_s^0 \to J/\psi f_2'(1525)$ and $B_s^0 \to J/\psi\phi$ in measured data are given by:

$$\epsilon_X = \epsilon_{geom} \cdot \epsilon_{MC} \cdot \epsilon_{PID}. \tag{6.3}$$

The numerical values of the total efficiency are summarized in Table 6.3.

Table 6.3: Total efficiency for both of the two considered decay modes.

Decay Mode	ϵ_X
$B_s^0 \to J/\psi f_2'(1525)$	0.93 ± 0.01 %
$B_s^0 \to J/\psi\phi$	1.10 ± 0.03 %

As a cross-check the efficiency for the $B_s^0 \to J/\psi\phi$ channel was also calculated with the $B_s^0 \to J/\psi\phi$ MC sample. Applying the same procedures this gives $\epsilon_\phi = (1.12 \pm 0.01)\%$ in perfect agreement with the value obtained from the non-resonant $B_s^0 \to J/\psi K^+K^-$-MC. It is therefor reasoned that the values in Table 6.3 are indeed the correct ones also for the $B_s^0 \to J/\psi f_2'(1525)$ channel.

Strictly speaking, additional studies concerning systematic differences between the measured data and the simulation would be necessary. Only that way it could be made absolutely sure that the efficiency values are indeed transferable. For example, it is not clear that the detector acceptance is described well by the simulation. However, the two studied decay modes are kinematically very similar and it can be assumed that the unconsidered systematic effects are very similar for both, too. When calculating the relative efficiency they should cancel out for the most part. Consequently, they do not have a large impact on the relative branching fraction because it only depends on the relative efficiency.

7 Final Result and Conclusion

From the results that have been discussed so far, the relative branching fraction $\mathcal{R}_{f_2'/\phi}$ of the decay mode $B_s^0 \to J/\psi f_2'(1525)$ with respect to $B_s^0 \to J/\psi\phi$ can be calculated. According to Equation (5.2), $\mathcal{R}_{f_2'/\phi}$ depends on the relative event yields and the relative efficiencies for both decay modes. The number of $f_2'(1525)$-events, $N_{f_2'} = 2187 \pm 111$, and the number of ϕ-events, $N_\phi = 13519 \pm 149$, were measured in Section 5. This was done by fitting the distributions of the invariant K^+K^- mass and the B_s^0 candidate's mass in a two-dimensional fit. The ratio is $N_{f_2'}/N_\phi = (16.18 \pm 0.84(stat.)^{+2.02}_{-1.18}(fit.))$ %, where the second error was estimated by varying the fit model.

The efficiencies for the decays $B_s^0 \to J/\psi f_2'(1525)$ and $B_s^0 \to J/\psi\phi$ were determined in Section 6 using a simulation of the non-resonant decay $B_s^0 \to J/\psi K^+K^-$. The

total efficiency was found to be $\epsilon_{f_2'} = (0.93 \pm 0.01)$ % for $B_s^0 \to J/\psi f_2'(1525)$ and $\epsilon_\phi = (1.10 \pm 0.03)$ % for $B_s^0 \to J/\psi\phi$. The errors are purely statistical. Systematic effects were not analyzed because it is assumed that they cancel out in the ratio $\epsilon_{f_2'}/\epsilon_\phi = (0.85 \pm 0.02)$ for the most part.

Finally the relative branching fraction also depends on the explicit branching fractions for the $f_2'(1525)$ and ϕ decaying into the considered K^+K^- final state. Those branching fractions have not been measured in this analysis and the PDG values are used: $\mathcal{B}(f_2'(1525) \to K^+K^-) = (44.4 \pm 1.1)$ % and $\mathcal{B}(\phi \to K^+K^-) = (48.9 \pm 0.5)$ % [11]. Inserting all those values in Equation (5.2) gives:

$$\mathcal{R}_{f_2'/\phi} = (21.07 \pm 1.26(stat.)\, ^{+2.63}_{-1.54}(fit) \pm 0.58(PDG))\ \% \tag{7.1}$$

The first error is purely statistical, the second one considers the variation of the relative event yields due to slight changes in the fit model and the third one contains the uncertainties of the used PDG values.

The ratio has previously been measured to $(26.4 \pm 2.7(stat.) \pm 2.4(syst.))$ % [5] which is in agreement within 2σ if only the statistical errors are considered. The difference in the size of the statistical error is due to different sizes of the data samples used for the analyses.

From this point on, there are various possibilities to continue with the analysis. First of all, systematic effects that could contribute an uncertainty to the relative branching fraction could be studied more deeply. In this thesis only the effect of the fit model was analyzed. In addition, it could be checked how the chosen mass range affects the fit results. Also, the background should be analyzed more accurately. It is known that there are physical background components from inclusive $B \to J/\psi X$ decays peaking in the B_s^0 as well as in either the $f_2'(1525)$ or the ϕ mass peak [5]. It was assumed that such background events were rejected by the selection requirements. This however, was not explicitly tested. Finally, it would be useful to have a simulation of the $B_s^0 \to J/\psi f_2'(1525)$ decay to cross-check the efficiency determined with the $B_s^0 \to J/\psi K^+K^-$-MC.

Besides the relative branching fraction, also other properties of the $B_s^0 \to J/\psi f_2'(1525)$ channel, like the angular distributions, could be analyzed. Or, the third mass peak that was observed in the $m(K^+K^-)$ distribution could be investigated more deeply. It would be interesting to see whether it really gives rise to an unobserved decay mode like $B_s^0 \to J/\psi f_0(1710)$.

References

[1] A. Sakharov, *Violation of CP Invariance, c Asymmetry, and Baryon Asymmetry of the Universe*, vol. 5, pp. 24–27. JETP Letters, 1967.

[2] J. Frieman, M. Turner, and D. Huterer, "Dark energy and the accelerating universe", *arXiv:0803.0982* (Mar., 2008) . http://arxiv.org/abs/0803.0982. Ann.Rev.Astron.Astrophys.46:385-432,2008.

[3] P. W. Higgs, "Broken symmetries and the masses of gauge bosons", *Physical Review Letters* **13** no. 16, (Oct., 1964) 508–509. http://link.aps.org/doi/10.1103/PhysRevLett.13.508.

[4] **LHCb Collaboration**, B. Adeva *et al.*, "Roadmap for selected key measurements of LHCb", *arXiv:0912.4179* (Dec., 2009) . http://arxiv.org/abs/0912.4179.

[5] **LHCb Collaboration**, R. Aaij *et al.*, "Observation of $B_s \to J/\psi f_2'(1525)$ in $J/\psi K^+K^-$ final states", *Phys.Rev.Lett.* **108** (2012) 151801, arXiv:1112.4695 [hep-ex].

[6] D. H. Perkins, *Introduction To High Energy Physics*. Cambridge University Press, Apr., 2000.

[7] H. Fritzsch, M. Gell-Mann, and H. Leutwyler, "Advantages of the color octet gluon picture", *Physics Letters B* **47** no. 4, (Nov., 1973) 365–368. http://adsabs.harvard.edu/abs/1973PhLB...47..365F.

[8] S. L. Glashow, "Partial symmetries of weak interactions." http://inspirehep.net/record/4328.

[9] S. Weinberg, "A model of leptons", *Phys. Rev. Lett.* **19** (Nov, 1967) 1264–1266. http://link.aps.org/doi/10.1103/PhysRevLett.19.1264.

[10] A. Salam and J. C. Ward, "Electromagnetic and weak interactions", *Phys.Lett.* **13** (1964) 168–171.

[11] **Particle Data Group**, J. Beringer *et al. Phys.Rev.Lett.* **D86** (2012) 010001. http://pdg.lbl.gov.

[12] E. Lohrmann, *Hochenergiephysik*, ch. 1.6, pp. 30–31. Vieweg+Teubner Verlag, 5, überarb. u. erw. aufl. 2005 ed., Mar., 2005.

[13] "LHCb public website", June, 2012. http://lhcb-public.web.cern.ch/lhcb-public/.

[14] "LHC website", June, 2012. http://lhc.web.cern.ch/lhc/.

[15] **LHCb Collaboration**, A. A. Alves *et al.*, "The LHCb detector at the LHC", *Journal of Instrumentation* **3** no. 08, (Aug., 2008) S08005–S08005. http://iopscience.iop.org/1748-0221/3/08/S08005.

[16] "CERN public website", June, 2012]. http://public.web.cern.ch/public/.

[17] G. Musiol, *Kern- und Elementarteilchenphysik*, ch. 4.2, pp. 117–119. Harri Deutsch Verlag, 1995.

[18] **LHCb Collaboration**, R. Aaij and J. Albrecht, "Muon triggers in the high level trigger of LHCb", 2011. http://cdsweb.cern.ch/record/1384386.

[19] T. Sjöstrand and A. de Roeck, "Monte carlo generators for the lhc. mc generators for the lhc", 2005. CERN, Geneva, 4 - 7 Apr 2005.

[20] "PYTHIA", June, 2012. http://home.thep.lu.se/~torbjorn/Pythia.html.

[21] R. J. Barlow, *Statistics: A Guide to the Use of Statistical Methods in the Physical Sciences*, ch. 5.4, pp. 90–92. John Wiley and Sons, 1989.

[22] "PIDCalibPackage", June, 2012. https://twiki.cern.ch/twiki/bin/view/LHCb/PIDCalibPackage.

[23] "Generation tables of the used mc samples", June, 2012. http://lhcb-release-area.web.cern.ch/LHCb-release-area/DOC/STATISTICS/MC11STAT/B2Charm-WG/Generation_Beam3500GeV-md100-MC11-nu2.html.

Erklärung:

Ich versichere, dass ich diese Arbeit selbstständig verfasst habe und keine anderen als die angegebenen Quellen und Hilfsmittel benutzt habe.

Heidelberg, den (Datum) .....